Analyst

PAPER

View Article Online
View Journal



Cite this: DOI: 10.1039/d5an00949a

# Non-invasive detection of Oncostatin M and TNF-α in a microphysiological chip with embedded pH tuning capabilities

Daniele Bellisario,† Alessandra Calogiuri, *† Elisa Sciurti, Laura Blasi,* Vanessa Esposito, Flavio Casino, Pietro Siciliano, Antonio Della Torre and Luca Francioso

The detection of disease biomarkers is crucial in biomedical research, diagnostics and personalized medicine. However, challenges still exist for the multiple and simultaneous analysis of different biomarkers due to their low concentration, the complexity of the biofluids and the presence of multiple interfering components. The Surface Enhanced Raman Scattering (SERS) technique combines high sensitivity, specificity, non-interference by water and compatibility with transparent packaging materials, thus making it suitable for Organ-on-Chip (OoC) applications. One of the main limitations of SERS is the spectral overlap resulting from the binding of different analytes to the substrate, which makes it difficult to identify specific biomarkers. The proposed approach addresses this limitation by integrating a SERS platform, functionalized with 3-mercaptopropionic acid (3-MPA), within a microfluidic platform. The carboxylic groups on the SERS surface can selectively interact with biomolecules by modulating the pH of the medium *versus* the isoelectric points of the proteins, thus improving the analyte–surface interaction. The proposed SERS-on-chip detection system has been optimised for detection in Ham's F-12K cell culture medium, without serum supplementation, of two colorectal cancer biomarkers, also known to be involved in epithelial–mesenchymal transition (EMT): Oncostatin M (OSM) and Tumor Necrosis Factor alpha (TNF-α). Furthermore, a Machine Learning (ML) classification was exploited to improve data resolution and to limit the spectral overlap. pH modulation was performed at the chip level with an embedded microfluidic mixer, without affecting the cell culture chamber, and Raman spectra were acquired through the chip cover under controlled temperature conditions. Trained on single-biomarker spectra, the models were tested in complex, realistic scenarios with non-target or both biomarkers. This represents a challenging, previously unseen scenario during the training phase and is highly relevant for practical applications where multiple analytes coexist in complex biological matrices, highlighting current limitations in mixture scenarios.

Received 4th September 2025,
Accepted 26th March 2026

DOI: 10.1039/d5an00949a

rsc.li/analyst



## Introduction

The rapid, label-free detection of biomarkers is essential for point-of-care (PoC) diagnostics and personalised medicine. It allows for the timely and minimally invasive assessment of a patient's condition directly at the point of care.[1] However, the simultaneous and selective detection of multiple biomarkers remains difficult due to their low concentrations and the complexity of biological matrices, as well as the low sensitivity and high detection limit of such devices. In this context, surface-enhanced Raman scattering (SERS) represents a powerful analytical technique that offers high sensitivity, molecular specificity, and compatibility with PoC devices.[2] The integration of SERS with Principal Component Analysis (PCA) and Machine Learning (ML) algorithms also allows for robust discrimination between pathological and reference samples, facilitating binary "on/off" classifications suitable for rapid diagnostic contexts.[3] Although this technological architecture has already been proposed in combination with organ-on-chip (OoC) systems for non-invasive, *in situ* monitoring of analytes,[4–7] the present study focuses on demonstrating the feasibility of a PoC-oriented SERS platform capable of reliably detecting specific biomarkers in complex, serum-free culture media.

Among non-invasive techniques, Raman spectroscopy can provide unambiguous information about the chemical composition of different samples, enabling qualitative and quantitative analyses of each individual sample. An increasingly

*Institute for Microelectronics and Microsystems CNR-IMM, Via per Monteroni "Campus Ecotekne", Lecce, Italy. E-mail: alessandracalogiuri@cnr.it, laura.blasi@cnr.it*

† The first two authors contributed equally to this work.

popular variant of Raman microspectroscopy is surface-enhanced Raman scattering (SERS). SERS is a powerful analytical technique that uses plasmonic analysis to accurately detect molecules absorbed or bound to nanostructured metal surfaces. It is a powerful and sensitive tool for the detection of chemical and biological analytes. It is a non-destructive analysis with high sensitivity, specificity, and accuracy and it represents a promising tool that can replace the traditional techniques used for the chemical–biological detection of analytes. SERS typically exploits the Raman signal enhancement of molecules that are close to plasmonic nanostructures. Therefore, this technique allows the rapid, simultaneous and non-destructive identification of several molecules.[2] Moreover, SERS achieves a signal enhancement of over 10 orders of magnitude compared to that of classical Raman microspectroscopy, and the electromagnetic effect is the main contributor to the signal enhancement.[8] Gold and silver nanoparticles, as active nanostructures in SERS substrates, enhance the Raman signal of different biological components, providing useful information on cell composition and monitoring specific biological properties of biological samples.[9,10] In addition, the SERS substrate can be designed and refined for near-infrared light sources to overcome the autofluorescence of biological samples and reduce laser damage to living cells. These advantages have encouraged the successful and non-invasive detection of biological molecules, pathogens, and *in vivo* cancer imaging.[8,11] However, when analysing complex media (*e.g.*, blood, plasma, saliva and urine), obtaining the SERS signal of the target analyte with sensitivity and accuracy is significantly hindered. In this context, integration within a microfluidic device facilitates the generation of a more reliable SERS signal and a highly effective detection. Moreover, microfluidics allows the precise control of small volumes of liquid samples, greatly improving the detection of the SERS signal.[12] Furthermore, pH affects protein conformation and surface charge and therefore it is a critical parameter that can significantly influence the interaction between the target and the active surface.[13] It is well known from the literature that the pH influences the charged substrates such as the effects on protonation/deprotonation of the terminal functional group, the different interfacial distribution of ions, the change in the net charge of ionizable molecules and the modified affinity for targets.[14–16]

In the present study, the embedding of a SERS substrate in a dedicated chamber of the microfluidic chip (Fig. 1) enables the modification of pH levels directly in the sensing chamber, without affecting the medium or the integrity of the culture chamber. Furthermore, the SERS substrate has been functionalized with a self-assembled monolayer (SAM) using 3-mercaptopropionic acid (3-MPA). Due to its short alkyl chain, 3-MPA minimizes steric hindrance and positions the analyte close to the SERS hotspots, thereby maximizing electromagnetic enhancement compared to longer chain thiols.[17] While the ionizable carboxyl groups of 3-MPA can modulate analyte–surface interactions through pH tuning relative to the proteins' isoelectric points, this strategy primarily enhances adsorption stability and can help reduce spectral overlap. Competitive adsorption, the intrinsic heterogeneity of SERS hotspots, and pH-dependent variations in protein charge and conformation may still contribute to spectral variability.

To enhance signal classification performance in label-free measurements, Machine Learning (ML) algorithms were exploited. This synergetic approach adopting microfluidics, on-chip SERS and machine learning (ML) algorithms allowed us to detect two target analytes in complex solutions. Specifically, our device allowed us to detect Oncostatin M (OSM) and Tumor Necrosis Factor alpha (TNF-α) in F12K commercial medium in a custom designed microfluidic device that can host multiple experiments and cell cultures on a porous PET support (Fig. 1). As a first proof-of-concept, no cells were included in the system and the medium was used without fetal bovine serum (FBS) supplementation in order to avoid introducing additional biological complexity and focus on validating the sensing platform under controlled conditions.

The present developed chip could be exploited for future *in vitro* studies on the induction of epithelial–mesenchymal transition (EMT), in which OSM is frequently used to stimulate specific cellular responses, such as the modulation of mesenchymal markers, the reduction of E-cadherin expression, and the increase in cell migratory capacity.[18] Furthermore, several studies have demonstrated the key role of OSM in regulating cellular plasticity,[19] in the acute inflammatory response, and in fibrosis processes, which suggests potential implications in various pathologies, such as renal and chronic inflammatory diseases.[20] In this study, a concentration of 25 ng $mL^{-1}$ OSM was chosen, a value frequently used in *in vitro* studies to ensure an adequate cellular response while maintaining controlled and reproducible experimental conditions.[19,20] TNF-α is an essential pro-inflammatory biomarker whose release varies depending on the cell type, for example, in microglia, TNF-α has been observed to increase from approximately 15 pg $mL^{-1}$ to 74 pg $mL^{-1}$ within 24 hours following NF-κB activation.[21] In EMT models using epithelial cells, OSM complexly modulates inflammatory signals. Indeed, Sarközi *et al.* reported that OSM interacts with the TNF-α pathway and contributes to the modulation of cellular plasticity during EMT.[22]

A significant challenge in the present study, which is based on a real-time, non-invasive, label-free SERS-based detection system, was the validation of a limited reusable system.[23] After the detection of the analytes of interest, the SERS platform was successfully made free from protein residuals, enabling the re-utilisation of the same device for multiple analysis cycles. The overcoming of these limitations, as well as the high cost of disposable substrates, strengthens the potential of this measurement tool, making it increasingly suitable for practical applications. This surface recovery process is mandatory to guarantee continuous monitoring inside the chip, and we will take this into account despite being aware of the effect. The authors demonstrated a technical solution to achieve partial platform reusability, considering that neither the chip can be

 

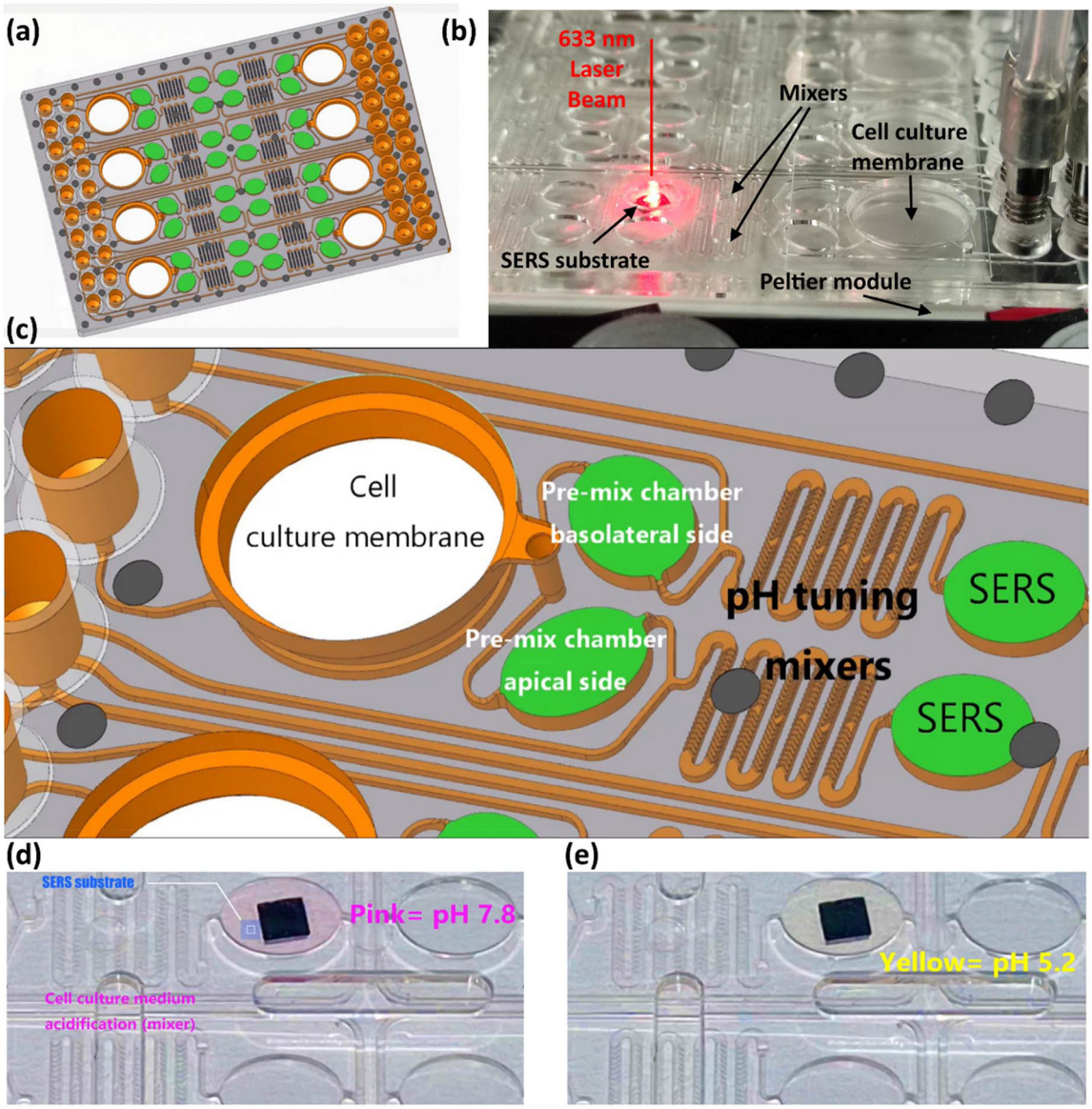


**Fig. 1** (a) 3D design of the developed microphysiological platform. (b) Photograph showing our experimental system for SERS spectrum acquisition equipped with Peltier-based temperature control (set to 37 °C). (c) Detailed layout of a single module, designed to study the epithelial barrier, comprising a cell culture chamber divided into apical and basolateral compartments by a PET membrane and two pre-mix chambers. Upstream of the mixers, an inlet for the pH tuning solution, enables autonomous pH adjustment in the measurement chambers, where the SERS substrates are located, without affecting the cell culture. Photograph showing the pH color shift (d) before the addition of the acid solution (e) and after the addition.

opened nor the substrate can be replaced during the experiment.

## Experimental

### Materials and methods

Commercially available Au SERS substrates "SERStrates", with an active area of 25 $mm^2$ consisting of approximately 600 nm height nanopillars on a silicon substrate, were purchased from Silmeco ApS (Copenhagen, Denmark). Ham's F-12K (Kaighn's) Medium (F12K) and phosphate buffered saline (PBS, liquid, sterile-filtered, suitable for cell culture) were purchased from Sigma Aldrich (St Louis, MO, United States). Human Oncostatin M Recombinant Protein (OSM) (Cat. PHC5015, no. L0216072020) was purchased from Gibco (Carlsbad, CA, USA). It was diluted in F12K medium and PBS at a ratio of 1 : 1 to achieve a final concentration of 25 ng $mL^{-1}$. Human TNF-α Recombinant Protein (TNF-α) (Cat. 300-01A, no. L041525) was purchased from PeproTech (Rocky Hill, NJ, USA). It was diluted in F12K medium and the diluent buffer from the Human TNF-α ELISA kit (Cat. 950.090.096, Diaclone SAS,

Besançon Cedex, France) (1× working solution) at a ratio of 1 : 1 to reach a final concentration of 100 pg $mL^{-1}$.

### Concept and layout of the microfluidic platform

Our microphysiological platform (OoC) has been designed to allow 8 independent experiments and is equipped with 8 double-sectioned chambers with apical and basolateral sides separated by a 23 micron thick, porous PET membrane (0.4 micron pores) that allows the seeding and growth of cell cultures and co-cultures of epithelial and endothelial lines (Fig. 1). The chip also has two separate mixers for each compartment (16 mixers), which allow titration of the medium coming out of the culture chambers *via* the auxiliary mixer input with acidic or basic solutions so that the measurement can then be performed in a dedicated chamber at optimal pH (Fig. 1, for the 3D layout of the device). The SERS substrate is housed in the chamber with a SERS label (Fig. 1b), and it was illuminated with a 633 nm He–Ne laser from the top cover. The chip was designed at the CNR-IMM institute and was manufactured by means of industrial mold-injection techniques using a TOPAS – cyclic olefin copolymer (COC). The chip is equipped with 40 mini-Luer ports (In, Out, Waste, Mixers secondary inlet) to allow fluidic connections to flow controllers or to allow membrane mechanical deflection *via* imposed pressure gradients.

### Functionalization of substrates

Before functionalization, the commercial gold substrates were gently rinsed with pure ethanol as a cleaning step. After the rinsing, a small droplet of DI water was deposited onto the substrate and left to evaporate. During evaporation, the surface tension causes the nanopillars to lean towards their nearest neighbours, thus creating self-assembled "hot spots".[24] In this case the nanopillars are permanently tilted prior to analyte exposure. The pre-leading strategy used typically exhibits an enhancement factor (EF) on the order of $10^6$ for these gold-coated pillar commercial substrates.[24] Afterward, carboxyl-terminated self-assembled monolayers (SAMs) were formed by immersing the cleaned SERS substrate in a 1 mM solution of 3-MPA in pure ethanol at room temperature for 24 hours, after previously adjusting the solution's pH to 2 using 10% acetic acid (v/v). After the soaking phase, the substrates underwent a sequential rinsing process, first with pure ethanol, then with distilled water, and finally with another rinsing with pure ethanol. The substrates were then stored in a clean, sealed container. Before use, the substrates were subjected to another sequential rinsing with pure ethanol, distilled water, and pure ethanol, following the same protocol reported above. Representative off-chip spectra of the bare commercial substrate and the 3-MPA-functionalized substrate are shown in SI (Fig. S1).

### Analytes off-chip reference spectra acquisition

To obtain reference spectra and assist in peak assignment for the target proteins, off-chip control experiments were conducted on 3-MPA functionalized substrates. The analyte solutions were prepared in PBS (pH 7.4) and analyzed on separate substrates for OSM and TNF-α. Higher analyte concentrations (OSM 20 μg $mL^{-1}$; TNF-α 800 pg $mL^{-1}$) were employed to enhance Raman signal visibility. For each analyte, spectra were first recorded from the functionalized substrate alone and then from the same type of substrate after evaporation of a droplet of analyte solution. Identical optical settings were used as in the on-chip experiments. A total of 128 spectra were acquired per analyte from different spots on the substrates (64 per condition) and processed as described below. Discriminative Raman shifts were determined through statistical comparison of spectra, using the natural logarithm of *p*-values, and tentatively assigned by referencing literature and spectral databases. The assigned peaks are listed in Table S1 (OSM) and Table S2 (TNF-α).

### On-chip pH tuning experiments

The pH tuning experiments were carried out under controlled conditions at 37 °C for all acquisitions, directly on-chip by exploiting the integrated microfluidic mixers. The delivery of acidic or basic solutions was combined with the medium stream at controlled flow rate ratios, allowing precise adjustment of the pH in the sensing chamber. The flow rates of the medium and the titrating solutions were regulated prior to the spectral acquisitions, ensuring that the desired pH was reached and stabilized before data collection. The effective pH of the solution leaving the sensing chamber was experimentally verified. The outlet medium was collected and analyzed with a benchtop pH meter to confirm the actual pH achieved after flowing through the sensing chamber. The flow rates of the acidic and basic inlet streams were fine-tuned until the desired pH value was measured at the chamber outlet. This on-chip mixing approach enabled accurate control of the experimental conditions without affecting the culture chamber. Between consecutive acquisition sets performed on the same SERS substrate, the sensing chamber was partially regenerated by flushing the microfluidic channel network with 80% (v/v) acetone for 20 min, followed by flushing with medium until complete removal of residual solvent prior to resuming spectral acquisition.

### Enzyme-linked immunosorbent assay (ELISA)

Enzyme-linked immunosorbent assay (ELISA) was performed to quantitatively evaluate the amount of OSM and TNF-α bound to the SERS substrates before and after the acetone washing step. SERS substrates were functionalized following the protocol described above. For TNF-α detection, functionalized SERS substrates were exposed to TNF-α for 45 min and subsequently treated with 100 μL of biotinylated anti-TNF-α antibody for 3 h. The substrates were then incubated with 100 μL of horseradish peroxidase (HRP)-conjugated streptavidin for 30 min. Colorimetric detection was initiated by adding 100 μL of 3,3′,5,5′-tetramethylbenzidine (TMB) solution. The reaction solution was carefully aspirated and transferred to a standard 96-well plate, and the absorbance was measured at 450 nm according to the manufacturer's instructions.

Analogously, SERS substrates were exposed to OSM for 45 min, incubated with 100 μL of biotinylated anti-OSM antibody for 1 h and then with 100 μL of HRP-conjugated streptavidin for 45 min. After the addition of 100 μL of TMB solution, the reaction solution was transferred to a 96-well plate and absorbance was recorded at 450 nm. To evaluate protein removal, the SERS substrates exposed to TNF-α or OSM were washed with 80% (v/v) acetone and the ELISA procedure was repeated following the same protocol. ELISA experimental results are reported in the SI.

### XPS measurement setup

X-ray photoelectron spectroscopy (XPS) measurements were performed using a Phoibos150 (Specs) photoelectron spectrometer with an Al Kα source (1486.61 eV) operating at 200 W and 15 kV on bare and functionalized SERS substrates, following the protocol described above. Base pressure in the analysis chamber was $7 \times 10^{-9}$ mbar. Wide scans and detailed spectra were acquired in fixed analyser transmission mode, utilizing a pass energy of 100 eV and a 1 eV step for the survey scan, while for high-resolution spectra, a pass energy of 30 eV and a 0.05 eV step were used. The spectra were processed using CasaXPS software, Version 2.3.26PR1.0. The binding energy scale was referenced to the adventitious C 1s peak (284.8 eV).

### SERS measurement setup

SERS spectra were recorded using a Raman microspectroscopy system consisting of an imaging spectrometer (iHR320 from Horiba Jobin Yvon, with a Syncerity cooled detector) coupled to a Zeiss Axio Imager M2 (Carl Zeiss Microscopy, LLC, White Plains, NY, USA). The setup was equipped with a 633 nm He–Ne laser operating at a power of 17 mW and a 200 μm entrance slit for the spectrometer (Fig. 2). A diffraction grating with 1800 grooves per mm was employed. Raman measurements were acquired using LabSpec 6.7 Spectroscopy Suite Software (Horiba Jobin Yvon). Before each use, the spectrometer was calibrated using a silicon wafer. The Raman spectra were recorded by focusing the laser on the gold substrates, acquiring data from an 8 × 8 point grid using a 20× objective in the Raman shift range from 600 to 1800 $cm^{-1}$ (5 s integration time, 3 accumulations).

### Data analysis

The acquired spectra were pre-processed and analyzed using Microcal Origin Pro 2023 software. This involved removing random cosmic ray peaks, followed by the application of a Savitzky–Golay filter with a second-order polynomial and a 50-point window. Baseline correction was then performed using the Asymmetrical Least Squares Smoothing algorithm with a smoothing factor of 4, effectively reducing external influences like autofluorescence. Finally, Standard Normal Variate (SNV) normalization was applied to the acquired spectra.[25–27] The data were analyzed by Principal Components Analysis (PCA), and the spectra were represented along the first 2 principal components vectors in the score plot. The examination of the scores provided information on the grouping and separation of spectra according to experimental conditions, while the loading plots were used to identify the Raman shifts that contributed most to the observed variance and class separation. These features correspond to the wavenumbers most responsible for discriminating between spectral classes.[28] The Peak Analyzer tool in OriginPro software was used to determine and mark both ordinary and hidden peaks. Then, the second-order derivative of each data point was calculated, followed by the application of quadratic Savitzky–Golay smoothing with a polynomial order of 2 and a window size of 5 points. Hidden peaks were identified by the presence of local maxima in the second-order derivative. To remove non-significant and randomly occurring peaks, we filtered those previously extracted based on their frequency of occurrence, considering a peak valid for each measurement set only if it appeared in at least half of the measurements within that set.

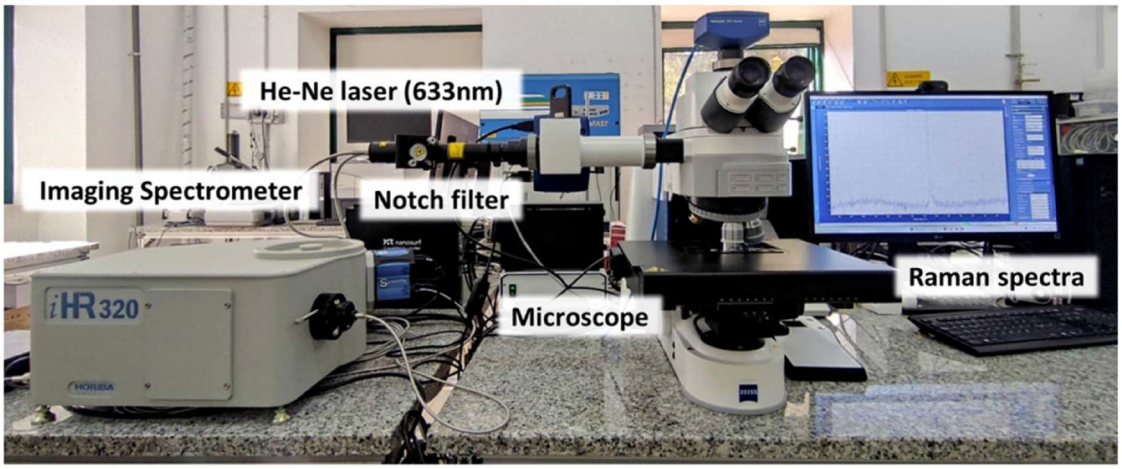


Fig. 2 Experimental setup for SERS analysis: a 633 nm He–Ne laser illuminates the sample through the microscope, while the scattered signal is filtered using a notch filter and directed to the iHR320 imaging spectrometer for Raman spectrum acquisition (Calogiuri *et al.*, (2024)[7]).

The significance of differences in the Raman signal between the different conditions was evaluated using an unpaired two-sample Student's *t*-test, with a significance threshold set at $1 \times 10^{-8}$. To highlight the discriminative Raman components, a logarithmic plot of the calculated *p*-values for each Raman intensity in the entire considered spectral range was generated.[29,30]

The extracted features were ranked by importance coefficients extracted by the training of a Linear Discriminant Analysis (LDA) and a linear SVM algorithm and then subsequently selected to obtain the optimal number of features that maximize the performance of the model.[31–34] Each acquisition was labelled and then randomly divided into two subsets:[35] 80% of the dataset was used as a training set and 20% of the dataset was used as a testing set. 10-Fold cross-validation for the validation step was chosen to avoid overfitting and the main hyperparameters used are shown in Table 1.

**Table 1** Main hyperparameters of the ML models used in this work with a split ratio of 80/20

| Model | Hyperparameter | Value |
|---|---|---|
| Quadratic SVM | Kernel | Poly |
| | Degree | 2 |
| | *C* | 1 |
| | Coef0 | 1 |
| | Gamma | Scale |
| Cubic SVM | Kernel | Poly |
| | Degree | 3 |
| | *C* | 1 |
| | Coef0 | 1 |
| | Gamma | Scale |
| Linear discriminant analysis | Solver | 1 |
| | Shrinkage | None |
| | *n*_Components | None |
| | Tol | 0.0001 |

Subsequently, the classifier was tested using one-fold, while the remaining $k - 1$ folds were employed for training. This procedure was repeated $k$ times, ensuring that each fold was used once as the test set.[36] This approach guarantees that every peak set in the dataset is utilized for both training and testing. The training accuracies, defined as the ratio between correctly classified spectra and the total number of spectra in the corresponding validation subset, were calculated as the average of the results obtained on the 10% of the training data held out during each iteration for testing.

## Results and discussion

### Functionalization assessment

Atomic Force Microscopy (AFM) measurements were carried out to verify changes in surface topography following 3-MPA functionalization. Gold nanostructured surfaces of the substrates have been functionalized by 3-MPA to form highly ordered SAMs with free carboxyl terminal groups. From AFM analysis (Fig. 3), it can be noted that the change of surface conformation due to 3-MPA functionalization modifies the surface morphology. Specifically, surface roughness is modified in a very remarkable way. Before golden surface functionalization (Fig. 3a) the roughness ($R_q$) is equal to 200 ± 16 nm. When the sample is treated in MPA (Fig. 3b) the roughness decreases, reaching a value of 130 ± 8 nm. This flattening could be interpreted as a sort of self-assembled connection among the nanopillars when MPA is adsorbed on gold in the acid medium through hydrogen bonds or electrostatic interaction.[37] The observed change in roughness could confirm the formation of a self-assembled layer of 3-MPA. Therefore, AFM provides supportive morphological evidence of surface modification.

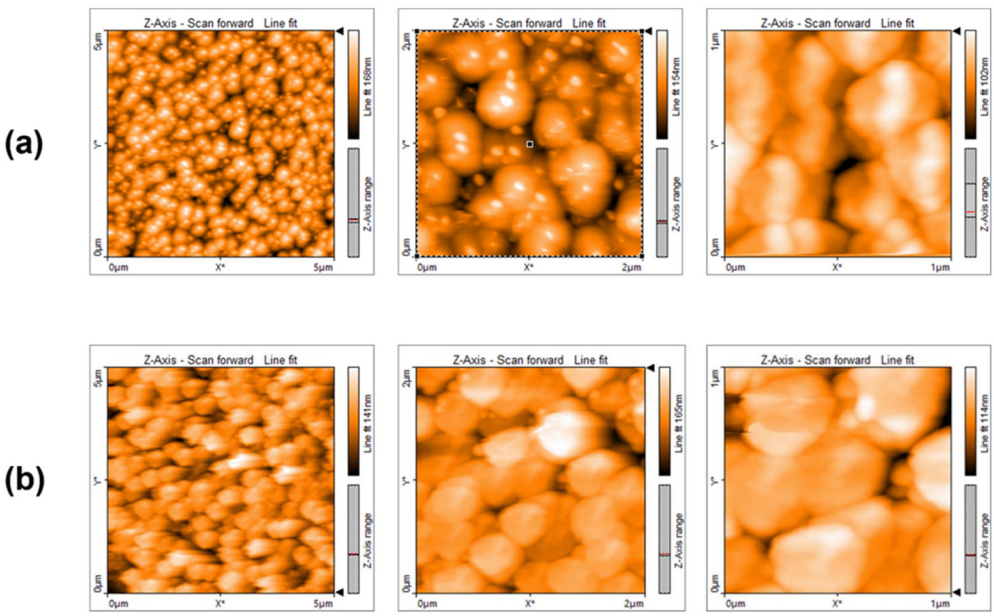


**Fig. 3** (a) Gold surface before the functionalization process; (b) gold surface after functionalization with 3-MPA.

XPS was used to assess the surface chemistry and the uniformity of the Au film. The investigated spectrum of bare gold is shown in Fig. 4a, where the spectral signatures, attributed to all expected elements, namely Au, C, and O, can be observed. Au was found to be the most abundant element. While the C1s and O1s peaks were ascribed to the natural surface hydrocarbon contamination of all samples exposed to air. The adsorption of 3-MPA on the gold surface was confirmed by the high resolution spectra of C1s and S2p. Fig. 4b shows XPS spectra of the C1s region for the 3-MPA/Au surfaces. It evidences the presence of characteristic peaks for the $-CH_2$ (284.8 eV), C–S (286.3 eV) and C═O (288.4 eV) groups.[38] While the high resolution S2p spectrum (Fig. 4c) displayed two doublets: a more abundant one, attributed to the covalently bonded Au thiolate (BES2 p3/2 = 162.3 eV), and a second one, attributed to the physisorbed thiolate (BES2 p3/2 = 163.6 eV).[39] This confirms the adsorption of 3-MPA on the gold surface. XPS analysis was also performed on the SERS substrates, following acetone washing, in order to provide a more comprehensive assessment of surface regeneration at the chemical level (Fig. S2).

### PCA results of a bare SERS substrate

The study initially evaluated the performance of unfunctionalized SERS substrates for the detection of OSM in F12K medium, focusing on the analyte at a chosen concentration (25 ng $ml^{-1}$). A total of 128 Raman spectra were subsequently acquired from different locations on the same functionalized SERS substrate, including 64 measurements with the F12K medium and 64 after the addition of OSM. After a preprocessing step, these spectra were compared using an unpaired two-sided Student's *t*-test performed on each Raman peak intensity, with a significance threshold set at $p < 1 \times 10^{-8}$ and $p < 1 \times 10^{-4}$.[29] As shown in Fig. 5a, adopting the more stringent threshold, no significant differences were observed for any of the analyzed Raman shifts, and only a single significant shift was identified at a lower threshold. This result is attributed to the spectral overlap caused by interfering components in the culture medium, which reduced the signal specificity and prevented accurate resolution of the target analyte's Raman signatures.[40] To further investigate the spectral overlap and its impact on distinguishing the presence of OSM, PCA was performed on the acquired Raman spectra.[41]

As shown in Fig. 5, the PCA score plots illustrate the relationships among the principal components PC1, PC2, and PC3. Specifically, Fig. 5 includes scatter plots of PC1 *vs.* PC2 (Fig. 5b), PC1 *vs.* PC3 (Fig. 5c), and PC2 *vs.* PC3 (Fig. 5d), which collectively represent the distribution of variance within the dataset. The explained variance for the first three principal components accounts for a total of 35.2% of the dataset variance. Despite this, the principal components failed to clearly separate the spectra of the F12K medium from those with the addition of OSM, indicating that key spectral features can be attenuated, too narrow or obscured by noise and interference from medium components.

### Identification of analyte fingerprints with 3-MPA functionalized substrates and high analyte concentrations

To improve the specificity of the analysis, a subsequent off-chip study as a reference control, focusing on the identification of Raman peaks with tentative assignments for both OSM and TNF-α, has been carried out. To further enhance the sensor's performance, the SERS surface was functionalized with 3-MPA to increase selectivity and analyte binding stability.[42] This functionalization aimed to reduce noise from the F12K medium, thereby allowing for more accurate and stable Raman signatures.[38] Therefore, a droplet of analyte solution was deposited onto the functionalized substrate and left to evaporate completely prior to spectral acquisition.

To amplify the Raman signals corresponding to the target molecules, higher analyte concentrations were exploited (OSM = 20 μg $ml^{-1}$; TNF-α = 800 pg $ml^{-1}$). For each analyte, spectra were acquired from a different functionalized SERS substrate, recording a total of 128 spectra per condition from different spots of the same substrate (F12K medium, $n$ = 64; F12K + analyte, $n$ = 64). The acquired spectra were then processed using the previously described preprocessing workflow. As illustrated in Fig. 6a and b, to identify the Raman peaks corresponding to OSM and TNF-α, examination of the natural logarithm of *p*-values calculated for each Raman shift was conducted. This method prioritized spectral regions where differences between the groups (F12K *vs.* F12K + analyte) were statistically significant, thus emphasizing variations induced by

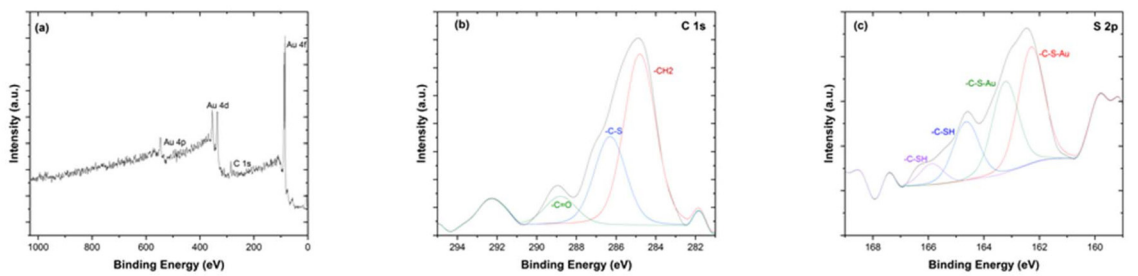


**Fig. 4** (a) Survey spectrum of bare gold with elemental signal assignments; (b and c) High-resolution spectra for C 1s and S 2p regions are reported with the curve-fitting results and peak component attributions.

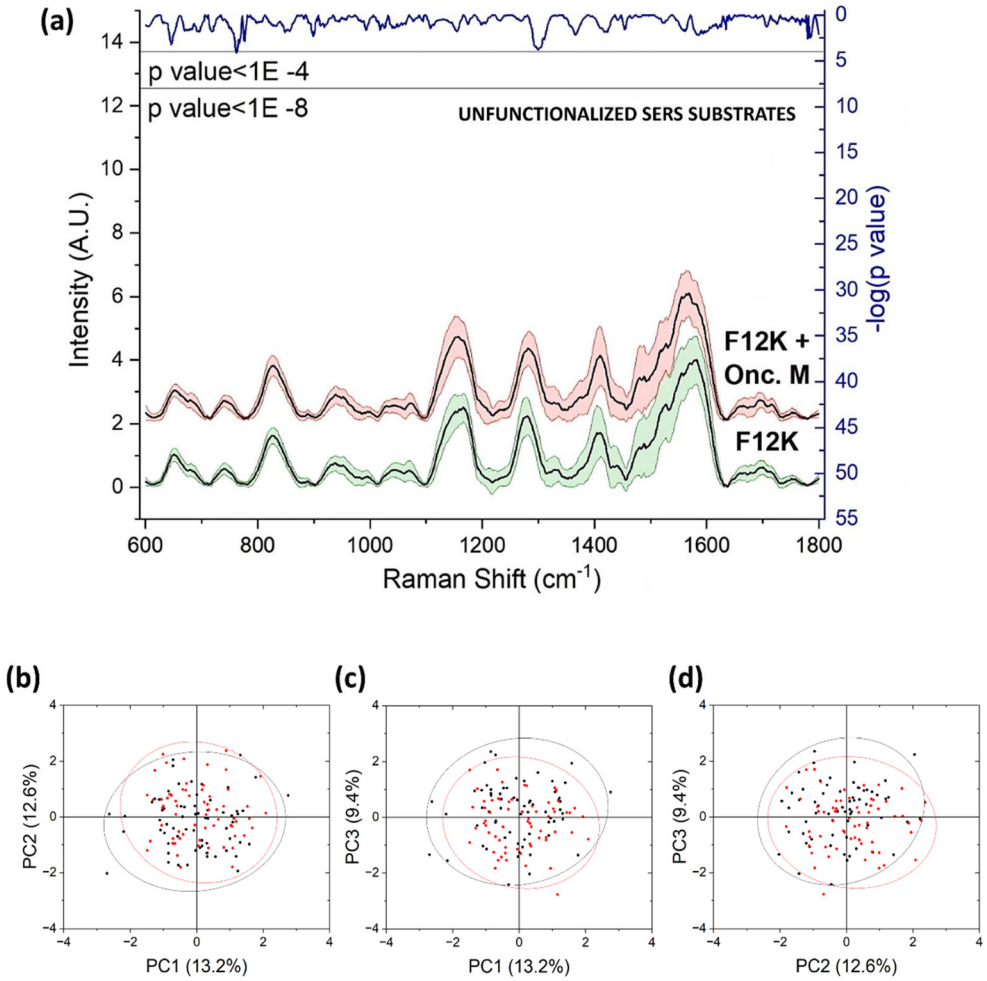


**Fig. 5** (a) Comparison of average Raman spectra acquired with unfunctionalized SERS substrates for F12K medium and F12K + Oncostatin M (25 ng ml$^{-1}$). Shaded areas represent the standard deviation. The blue line indicates the natural logarithm of *p*-values calculated for each Raman shift. No significant differences between the two groups were found. Principal Component Analysis (PCA) score plots of Raman spectra acquired with unfunctionalized SERS substrates for F12K medium [black dots] and F12K + Oncostatin M (25 ng ml$^{-1}$) [red dots]. Scatter plots show (b) PC1 *vs.* PC2, (c) PC1 *vs.* PC3, and (d) PC2 *vs.* PC3.

the presence of the analyte rather than background signals of the medium.[29] Peaks with high logarithmic *p*-values were considered candidates for tentative assignments. This strategy was adopted to emphasize statistically robust features, avoiding reliance exclusively on the average spectrum, which could obscure slight but meaningful differences. Positive peaks were identified from each acquisition by determining local maxima in the spectra and using the second derivative method, coupled with a quadratic Savitzky–Golay smoothing (window size of 5), to enhance peak detection while minimizing noise.[43,44] Each peak's intensity at its corresponding Raman shift was extracted, and only peaks occurring in at least 50% of the measurements for each condition (32 out of 64 spectra for each condition) were retained. Tentative assignments for these peaks were performed by comparing the observed Raman shifts with reference databases and literature values for functional groups, characteristic of OSM and TNF-α.[45–47] However, it should be acknowledged that the direct correspondence between Raman and SERS spectra must be interpreted with care, as factors such as molecular orientation, surface adsorption, and hotspot heterogeneity can induce peak shifts or intensity variations.[48] The peaks with $-\log(p\text{-value}) \geq 8$ were correlated with possible molecular vibrations, characteristic of the examined protein. A total of 24 peaks for OSM and 29 for TNF-α were respectively assigned and are presented in Tables S1 and S2, which list the corresponding Raman peaks and their associated molecular vibrations. It should also be noted that some of these spectral regions may also overlap with vibrations arising from components of the F12K culture medium such as free amino acids, lipids, and vitamins. However, the statistical approach adopted here isolates wavenumbers that significantly vary in the presence of the analyte, ensuring that the detected changes reflect analyte–surface interactions rather than the medium background. Some of the most interesting peaks found for OSM were in the region ranging from 680 to 850 cm$^{-1}$, characterized by a series of

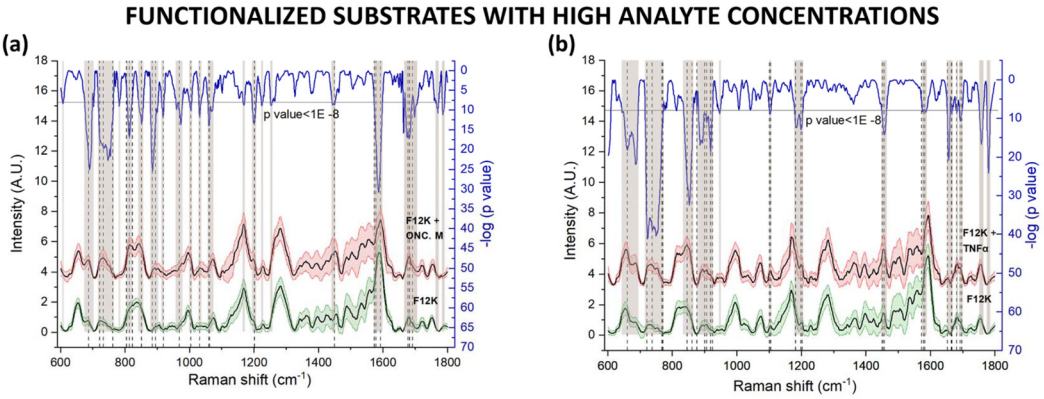


**Fig. 6** Average Raman spectra acquired with 3-MPA functionalized SERS substrates for (a) F12K + OSM (20 μg ml$^{-1}$) and (b) F12K + TNF-α (800 pg ml$^{-1}$). The natural logarithm of *p*-values calculated for each Raman shift is shown to identify peaks corresponding to the target analytes.

closely spaced and overlapping peaks. These can be associated with amino acids such as methionine, serine, tryptophan, proline, hydroxyproline and glutamine.[45,46] Additionally, peaks at 1573, 1579, and 1593 cm$^{-1}$ can be related to amide II vibrations, reflecting the protein's secondary structure. Moreover, peaks at 1678, 1683, and 1692 cm$^{-1}$ were mainly attributed to amide I,[46,47] highlighting the protein's structural complexity and amino acid composition. Similarly, the most statistically significant differences among the spectra acquired for TNF-α were observed at various shifts, including 661 cm$^{-1}$ associated with cysteine, 722 and 738 cm$^{-1}$ linked to sulfur-containing amino acids,[45] 877 cm$^{-1}$ assigned to hydroxyproline,[45] and a series of overlapping peaks in the region from 1653 cm$^{-1}$ to 1697 cm$^{-1}$, possibly corresponding to the amide I vibrations of proteins, which are primarily associated with the C═O stretching of the peptide backbone.[47]

### Enhanced discrimination capabilities of 3-MPA functionalized substrates with target concentrations

To further investigate the limitations of the bare SERS substrate and assess the impact of SAM functionalization, a comparative analysis was conducted exploiting the same experimental conditions of the bare SERS substrate analysis (previous section).[38,49] As in the previous analysis, 128 Raman spectra were subsequently acquired from different locations on the same functionalized SERS substrate (64 for F12K medium and 64 for F12K medium with OSM at 25 ng ml$^{-1}$) and processed with the same pipeline. Fig. 7a presents the mean spectra and standard deviations for the two groups (F12K medium and F12K + OSM) obtained with the functionalized SERS substrate. Additionally, the natural logarithm of the *p*-values from a two-sided unpaired Student's *t*-test is plotted, highlighting spectral regions with significant differences between the groups. The functionalized substrate exhibited clear improvements in spectral discrimination. The log-transformed *p*-values revealed several regions with highly significant differences ($-\log(p\text{-value}) \geq 8$), indicating that the functionalization enhanced the resolution of Raman peaks corresponding to OSM (Fig. 5 *vs*. Fig. 7). Statistically significant differences were observed in regions such as 700–850 cm$^{-1}$ and 1200–1700 cm$^{-1}$, corresponding to molecular vibrations of amino acids,[45,46] and structural elements of the protein (*e.g.*, amide and disordered structure signals).[46,47] These differences were either undetectable or masked in the unfunctionalized spectra.

To complement the spectral analysis, PCA was conducted on the spectra previously acquired. As illustrated in Fig. 7, the percentage of variance explained by the first three principal components (PCs) was comparable to the unfunctionalized case: PC1 accounted for 12.6%, PC2 for 12.5%, and PC3 for 9.9%, with a cumulative explained variance of 35.0%. Despite the similar variance distribution, the score plots revealed an improved class separation for the functionalized substrate. A slight separation between the two classes was visible in the PC1 *vs.* PC3 (Fig. 7c) plot, whereas the PC2 *vs.* PC3 (Fig. 7d) plot exhibited a more pronounced separation.

### OSM detection enhancement by pH tuning

The pH is a critical parameter that can significantly influence the spectroscopic measurements of biomolecules such as OSM and TNF-α. This effect is evident through various mechanisms, including alterations in protein conformation, surface charge, and interactions with functionalized SERS substrates.[14,15] Since many biomolecules contain ionizable functional groups, changes in pH can affect their physicochemical behaviour, thus modulating both biomolecules and surface functional groups, as well as their Raman fingerprints.[50–52]

In this study, pH optimization was exploited to maximize the specificity and intensity of the Raman signals for OSM and TNF-α. Different pH conditions were examined with the purpose of reducing noise from the F12K medium and enhancing the resolution of Raman peaks attributed to the analyte. Two sets of measurements were obtained from the same SERS substrate under the same conditions as the previous analysis, each consisting of 128 consecutive acquisitions separated by a wash in acetone for 20 minutes, resulting in a total of 256 spectra for each pH. The analyzed pH values for OSM were selected within a range spanning from its isoelectric point

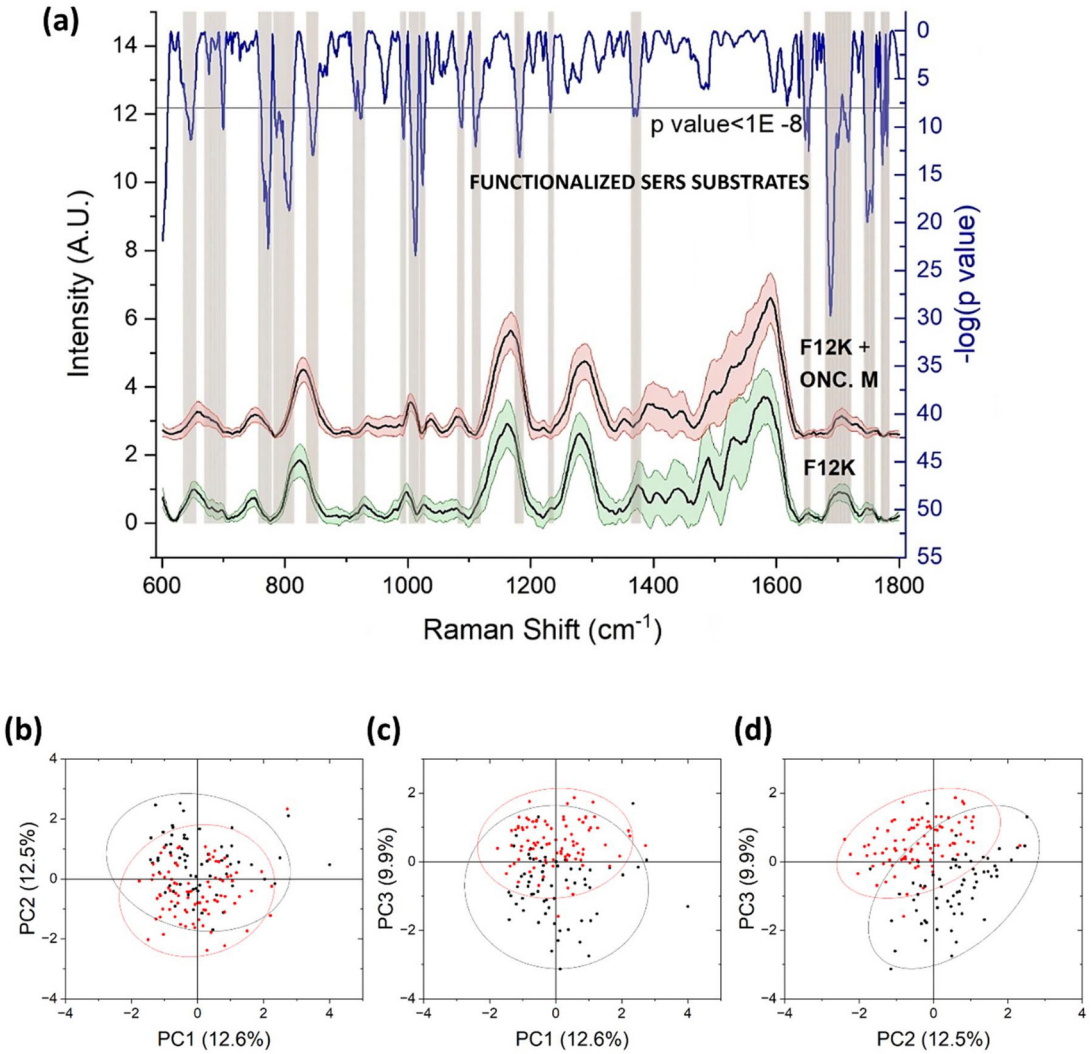


**Fig. 7** (a) Comparison of average Raman spectra acquired with 3-MPA functionalized SERS substrates for F12K medium and F12K + Oncostatin M (25 ng ml$^{-1}$). Shaded areas represent the standard deviation. The blue line indicates the natural logarithm of *p*-values calculated for each Raman shift. Significant differences between the two groups were found. Principal Component Analysis (PCA) score plots of Raman spectra acquired with 3-MPA functionalized SERS substrates for F12K medium [black dots] and F12K + Oncostatin M (25 ng ml$^{-1}$) [red dots]. Scatter plots show (b) PC1 *vs.* PC2, (c) PC1 *vs.* PC3, and (d) PC2 *vs.* PC3.

(10.6) and the apparent surface p$K_a$ of 3-MPA. The apparent surface p$K_a$ of 3-MPA varies with the roughness of the gold substrate, shifting by up to four units compared to its value (4.3) in free solution,[53] aiming to enhance the analyte binding to the substrate based on theoretical considerations of protonation and deprotonation, according to previous studies.[54,55] At pH values below the protein's isoelectric point, OSM is predominantly protonated and positively charged, whereas at pH values above the p$K_a$ of 3-MPA the terminal carboxyl groups deprotonate, imparting a negative charge to the substrate. This complementary charge distribution enhances electrostatic interactions, thereby leading to the most effective analyte binding. Such behaviour is demonstrated by research studies showing that protein adsorption and orientation on gold electrodes are highly sensitive to pH variations[14] and by theoretical models that attribute shifts in the apparent p$K_a$ of carboxyl-terminated self-assembled monolayers to coulombic interactions and hydrogen bonding[16] In addition, investigations on polymeric substrates have demonstrated that pH not only influences the protein adsorption but also alters the orientation and thickness of the adsorbed protein layer,[15] while studies on potential-driven deposition confirm that manipulating the ionization state of 3-MPA monolayers *via* applied potential can further optimize the electrostatic assembly.[56] Five of the analyzed pH values (8.5, 7.8, 7.4, 6.8, and 6.4) fall within this range, while pH 4 was deliberately chosen as an out-of-range condition to assess its impact on the analyte's spectral behaviour. The processed spectra were analyzed by PCA to investigate the effect of pH on the spectral features and to assess the influence of pH on the analyte–substrate interaction.

PCA analysis of the processed spectra revealed distinct spectral variations across the pH conditions. As shown in Fig. 8,

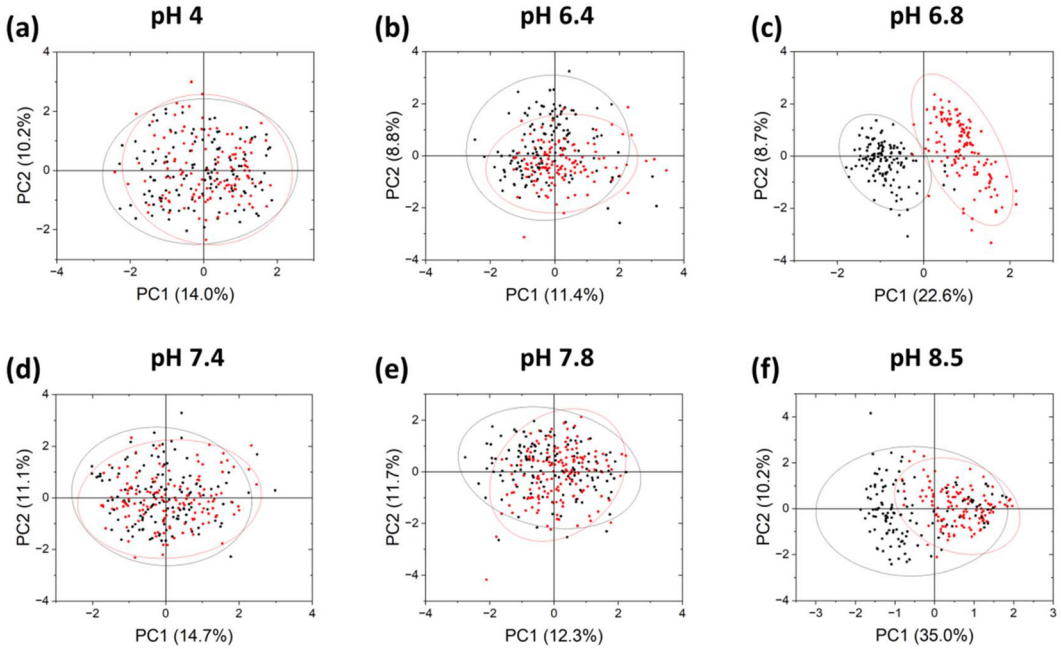


**Fig. 8** PCA score plots of Raman spectra acquired with 3-MPA functionalized SERS substrates for F12K medium [black dots] and F12K + OSM [red dots] at different pH values: (a) pH 4, (b) pH 6.4, (c) pH 6.8, (d) pH 7.4, (e) pH 7.8, and (f) pH 8.5. The score plots of the first two principal components indicate the most pronounced separation between the medium and the medium supplemented with OSM at pH 6.8 (c) and pH 8.5 (f).

the score plots of the first two principal components indicate the most pronounced separation between the medium and the medium supplemented with OSM at pH 6.8 (Fig. 8c) and pH 8.5 (Fig. 8f). In addition, it is worth noting that the PCA results and the absence of a monotonic trend may reflect the measurement sequence (including the intermediate acetone washing/regeneration step) as well as chip-to-chip variability across the tested pH conditions. Furthermore, because SERS preferentially probes moieties closest to the surface and within hotspots, small pH-driven changes in adsorption geometry and proximity can produce non-proportional spectral differences that obscure smooth pH trends in PC1–PC2, which may instead be captured in lower-variance components, partially masking part of electrostatic contribution.[8,10,46] The presence of two apparently distinct groups suggests that the acetone washing step could enable the system to partially return to initial conditions, thus allowing a second consecutive measurement to be carried out almost under comparable conditions. The failure to fully return to the initial conditions could indicate that bound molecules have not been removed completely or that SAM performances decreased during regeneration. ELISA tests carried out on OSM or TNF-α functionalized SERS substrates confirmed that the acetone washing step partially removes adsorbed proteins, thus enabling the reuse of the device (see the SI).

### TNF-α detection enhancement by pH tuning

Following a similar approach to that employed for OSM, we investigated the effect of pH on the SERS response to TNF-α, aiming to maximize the specificity and intensity of the protein's Raman signals. For this set of measurements, the TNF-α concentration in the F12K medium was 100 pg ml$^{-1}$, and the examined pH values spanned from 4.0 to 8.0 including the p$K_a$ of 3-MPA (5.2) and the isoelectric point of TNF-α (6.4), mirroring the experimental design already discussed for OSM while focusing on the specific behaviour of TNF-α. For each pH condition, two consecutive sets of measurements were acquired on the same SERS substrate, separated by an acetone wash, for a total of 256 acquisitions.

As shown in Fig. 9, which shows the PCA results, a clear separation between the F12K (control) and F12K + TNF-α groups was not consistently observed across the tested pH conditions, despite following the previously reported preprocessing pipeline. However, a moderate improvement in class separation emerged at the isoelectric point (pH 6.4, Fig. 9d), as well as at pH 7.0 (Fig. 9e) and 7.7 (Fig. 9g). In these cases, the PCA score plots revealed partially distinct clusters, although the explained variance of the first few principal components remained in the same range as previously found for OSM. As in the case of OSM, the PCA results suggest that acetone washing may partially restore the substrate for repeated acquisitions, and indeed no clear distinctions could be observed between spectra acquired before and after washing.

### Machine learning algorithm for identification of OSM and TNF-α above the cut-off concentrations

To develop a non-invasive PoC tool for improving on-chip antigen detection, these results were fed into a supervised classification algorithm in order to identify if OSM and TNF-α were above the cut-off concentrations (OSM/25 ng ml$^{-1}$ and

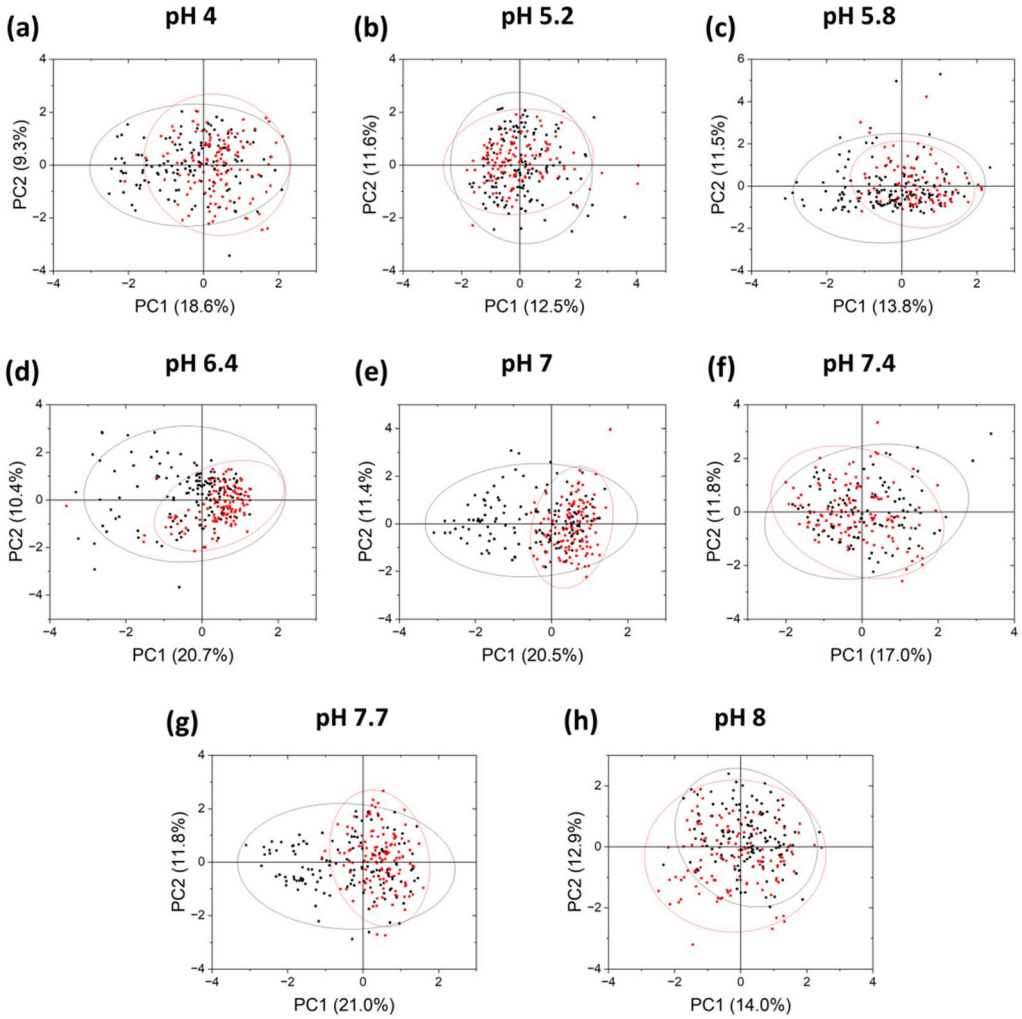


**Fig. 9** PCA score plots of Raman spectra acquired with 3-MPA functionalized SERS substrates for F12K medium [black dots] and F12K + TNF-α [red dots] at different pH values: (a) pH 4.0, (b) pH 5.2, (c) pH 5.8, (d) pH 6.4, (e) pH 7.0, (f) pH 7.4, (g) pH 7.7, and (h) pH 8.0.

TNF-α/100 pg $ml^{-1}$). This binary discrimination strategy, although simplified, reflects a clinically oriented point-of-care readout, rapidly indicating whether critical thresholds have been reached, and represents a first step toward more advanced quantitative models for continuous monitoring in future organ-on-chip applications. Furthermore, this study was conceived as a proof-of-concept to assess discriminative capability at representative biomarker concentrations. Accordingly, a full analytical characterization is beyond the present scope and will be addressed in future work.

### OSM classification – linear support vector machine (SVM) and linear discriminant analysis (LDA) results

Details of the data processing workflow are reported in the SI, paragraph "OSM classification – Linear Support Vector Machine (SVM) and Linear Discriminant Analysis (LDA) data processing".

As shown in Tables S3 and S4, models trained with features ranked using LDA exhibited a consistent improvement in accuracy as the number of features increased, reaching optimal classification performance with the top 100 features, particularly at pH 6.4, 6.8, and 8.5. Similarly, models utilizing SVM-ranked features generally benefit from an enlarged number of features but sometimes achieve comparable or superior accuracy with the top 40 features in both validation and test phases. However, slight declines in test accuracy were noted for SVM ranking models at pH 6.4 and 8.5. Confusion matrices for the OSM detection models with the highest accuracy in the test phase are also shown in Fig. S3 and S4.

Both approaches identified pH 6.8 and 8.5 as optimal conditions for classification, while pH 4 consistently yielded the lowest accuracy in both rankings, highlighting its limitations in providing distinguishable Raman signatures for effective discrimination. The loading plots of the first three principal components, as shown in Fig. S5, provide insight into the Raman shifts contributing to class separation for OSM detection at pH 6.8, further validating the peaks selected for model training. As shown in Fig. S5, PC1 captures stable structural

features of OSM, primarily associated with peaks at 805, 895, 1004, and 1450 $cm^{-1}$, which correspond to aromatic amino acids and $CH_2$ bending. In contrast, PC2 reflects, emphasizing peaks at 733, 763, 969, 1573, and 1579 $cm^{-1}$, linked to C–S stretching, tryptophan, and C–C stretching. Meanwhile, PC3 is associated with peaks at 919, 1032, 1678, and 1685 $cm^{-1}$, linked to proline, hydroxyproline, $CH_2CH_3$ bending modes, and amide I vibrations. These vibrations reflect pH-dependent structural rearrangements, particularly in secondary structure elements. Additionally, several peaks, including 688, 823, 852, 1202, and 1692 $cm^{-1}$, are shared across PCs, underscoring the role of proline, tyrosine, and amide I vibrations in capturing the pH-sensitive dynamics of OSM. These findings suggested that pH 6.8 for OSM provides optimal conditions for enhancing spectral resolution and improving classification accuracy.

### TNF-α classification – linear support vector machine (SVM) and linear discriminant analysis (LDA) results

Details of the data processing workflow are reported in the SI, paragraph "TNF-α classification – Linear Support Vector Machine (SVM) and Linear Discriminant Analysis (LDA) data processing". As shown in Tables S5 and S6, the best test accuracy was observed at pH 5.2, followed by pH 4, which showed significantly higher training results. In contrast, pH 8 consistently yielded the lowest test accuracy, followed by pH 7.7 and pH 5.8. A significant improvement in classification performance was observed with SVM-ranked features, as higher test accuracies were recorded across nearly all pH values except pH 7.4 and pH 8. Once again, pH 8 was confirmed as the condition with the weakest classification performance. Although pH 7.4 and pH 5.2 consistently stood out an excellent conditions and pH 7.7 also achieved some of the highest training and test accuracies. Remarkably, pH 4 yielded the highest training and test accuracies, achieving perfect classification during the test phase and thus confirming its potential to improve measurement conditions. In addition, confusion matrices for the TNF-α detection models with the highest accuracy in the test phase are shown in Fig. S6 and S7.

The loading plots of the first three principal components for TNF-α detection at pH 4, as shown in Fig. S8, highlight the Raman shifts contributing to class separation, further supporting the effectiveness of this pH condition. Most of the characteristic peaks of TNF-α are strongly associated with PC1, which are related to the primary structural features of the protein. This includes peaks linked to aromatic amino acids, C–C stretching, and amide I vibrations, reflecting stable conformational elements. Notably, 738, 901, and 907 $cm^{-1}$ are uniquely associated with PC1, indicating their relevance in capturing the core structural identity of TNF-α. In contrast, PC2 is linked to peaks at 1182, 1202, and 1583 $cm^{-1}$, corresponding to C–H bending and C=C bending modes. PC3 highlights vibrational modes at 660, 846, 861, 1101, 1105, 1198, 1202, 1579, 1692, and 1697 $cm^{-1}$, associated with C–S stretching, tyrosine, phenylalanine, and amide I vibrations. Uniquely, 1678 $cm^{-1}$ is present only in PC3, emphasizing its specificity in detecting β-sheet structures. Additionally, peaks at 1182, 1450, 1453, 1457, and 1570 $cm^{-1}$ are shared across all three PCs, underscoring their importance in capturing comprehensive structural information of TNF-α. These findings indicate that PC1 is most influential in defining the structural identity of TNF-α, while PC2 and PC3 contribute to detecting subtle pH-induced conformational changes.

### ML classification performance *vs.* OSM in F12K medium in the presence of both antigens

An additional analysis aimed at assessing the model's performance at the optimal pH (6.8) while also taking potential batch effects into account was carried out.[57,58] The training set was populated by measurements acquired from the same functionalized SERS substrate, totalling 384 spectra (64 from F12K medium and 64 from F12K medium with OSM at 25 ng $ml^{-1}$, collected from 3 different sets of measurements). An independent batch of 256 subsequent acquisitions, performed on a second SERS substrate, was exploited as the test set. In this test set, Class 0 represents spectra obtained in the absence of OSM and includes both F12K medium (64 acquisitions) and F12K medium with TNF-α (64 acquisitions). Conversely, Class 1 corresponds to spectra acquired in the presence of OSM, comprising both F12K medium with OSM (64 acquisitions) and F12K medium with TNF-α and OSM (64 acquisitions).[57] This classification strategy was designed to evaluate the model's ability to specifically distinguish the presence of OSM, even in complex biological environments where other analytes, such as TNF-α in our case, may be present. In this setting, spectra containing interferents were intentionally excluded from the training phase and used only for testing in order to challenge the model's generalization capability under the most demanding conditions. The peaks of each spectrum were extracted, filtered, and ranked according to the previously described procedure, and then considered for further analysis. The LDA and SVM ranked peaks underwent forward feature selection using a linear SVM model, which systematically explored combinations of features to optimize classification performance based on training accuracy.[59,60] To reduce computational effort, only the top 100 ranked peaks were considered. This iterative process incrementally evaluated different subsets of features, ranking their performance to identify those most significant for maximizing training accuracy. At the same time, the accuracy from the test phase was also evaluated for each subset.

As shown in Fig. 10, which presents the confusion matrices for both the training (Fig. 10a) and test (Fig. 10b) phases, the model, using 65 LDA-ranked features and following hyperparameter optimization, achieved a training accuracy of 85.5% and a test accuracy of 79.1%, thus demonstrating its robust generalization capability even in the presence of potential batch effects. These results highlight the model's effectiveness in distinguishing between classes under varying experimental conditions.

Detailed performance metrics, including precision, recall, and F1-score for both classes, are presented in Table 2, providing a comprehensive overview of the model's classification performance. In addition, the resulting optimized hyperpara-

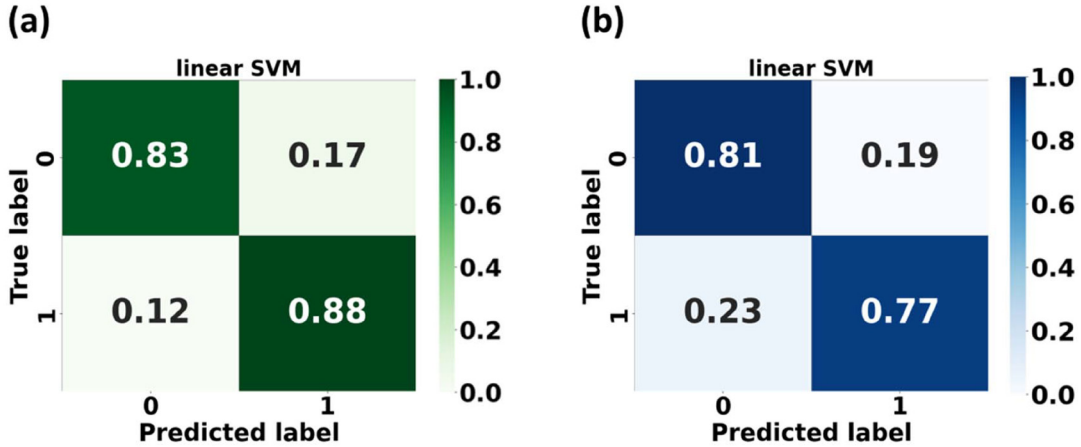


**Fig. 10** Confusion matrices for (a) training and (b) testing of linear SVM classification of OSM at optimal pH. The model used 65 top-ranked features after sequential feature selection and hyperparameter optimization.

meters are resumed in Table S7. To further evaluate class-specific performance, confusion matrices for each condition are shown in Fig. S9. The linear SVM model effectively distinguished OSM at the optimal pH of 6.8 under simpler conditions, achieving high accuracy in the F12K medium without OSM (87%) and with OSM (97%), demonstrating excellent specificity and sensitivity. However, performance declined in the presence of TNF-α, with accuracy dropping to 75% in the F12K medium with TNF-α and 58% when both TNF-α and OSM were present.

These findings suggest spectral interference or competitive adsorption at the SERS surface, leading to overlapping features and increased false negatives. The decline in accuracy is partly due to the model being trained only on spectra without interfering analytes, limiting its ability to generalize under more complex conditions. Including interferent-containing spectra in the training set could improve robustness and enhance the model's discrimination capability in complex biological environments. Despite these limitations, the linear SVM model demonstrated robust generalization under simpler conditions, confirming its potential utility for OSM detection in controlled experimental setups. Moreover, metrics are reported at the single-spectrum level; in practical deployments, the sample-level label would be derived by aggregating multiple spectra by majority voting, thereby improving reliability.[61]

### ML classification performance *vs.* TNF-α in F12K medium in the presence of both antigens

To assess the model's performance at the optimal pH value while accounting for potential batch effects, an additional analysis was conducted. The training set consisted of 256 spectra acquired from two sets of measurements on the same functionalized SERS substrate, including 128 spectra from the F12K medium and 128 spectra from the F12K medium supplemented with TNF-α at 100 pg $ml^{-1}$. A separate test set of 256 spectra was recorded from a second SERS substrate to evaluate generalization. In the test set, Class 0 represents spectra recorded in the absence of TNF-α, comprising both the F12K medium (64 acquisitions) and the F12K medium with OSM (64 acquisitions). On the other hand, Class 1 includes spectra acquired in the presence of TNF-α, comprising both the F12K medium with TNF-α (64 acquisitions) and the F12K medium with TNF-α and OSM (64 acquisitions). Following the same procedure described for OSM, the model's generalization ability was challenged by excluding interferent-containing spectra from the training phase and using them only for testing. After the peaks' extraction, filtering, and ranking, forward feature selection was subsequently applied to identify the optimal subset of features for classification. As shown in Fig. 11, which presents the confusion matrices for both the training (Fig. 11a) and test (Fig. 11b) phases, the model, using 55 LDA-ranked features and following hyperparameter optimization, obtained a training accuracy of 100.0% and a test accuracy of 77.1%, showcasing its high discriminative power, despite potential batch effects. These results underscore the model's ability to distinguish between classes even under different experimental conditions.

Detailed performance metrics, including specificity, precision, sensitivity, and F1-score for both classes, are presented in Table 3, offering a comprehensive overview of the model's classification performance.

**Table 2** Performance metrics of the OSM model obtained at optimal pH. Metrics include train accuracy, test accuracy, specificity, precision, sensitivity (recall), and F1 score

| Target | pH | Model | No. of features | Specificity | Precision | Sensitivity | F1_score | Train accuracy | Test accuracy |
|---|---|---|---|---|---|---|---|---|---|
| OSM | 6.8 | Linear SVM | 65 | 0.81 | 0.805 | 0.773 | 0.789 | 85.5% | 79.1% |

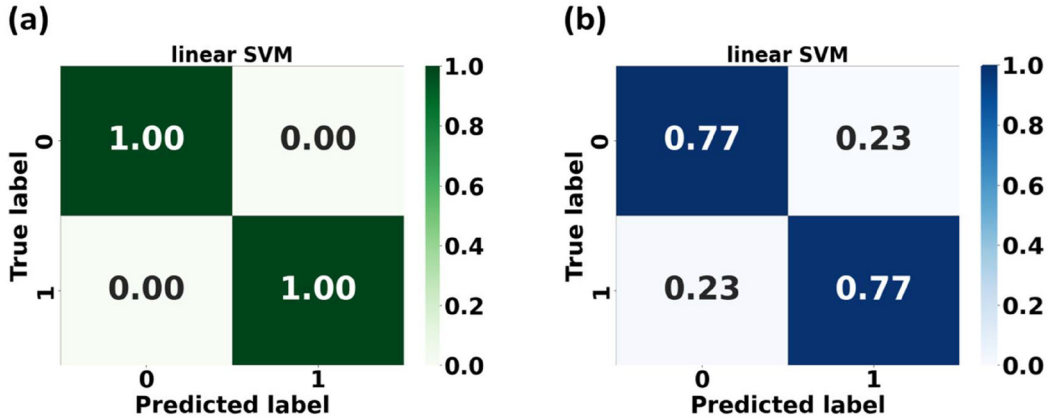


Fig. 11 Confusion matrices for (a) training and (b) testing of linear SVM classification of TNF-α at optimal pH. The model used 55 top-ranked features after sequential feature selection and hyperparameter optimization.

Table 3 Performance metrics of the TNF-α model obtained at optimal pH. Metrics include train accuracy, test accuracy, specificity, precision, sensitivity (recall), and F1 score

| Target | pH | Model | No. of features | Specificity | Precision | Sensitivity | F1_score | Train accuracy | Test accuracy |
|---|---|---|---|---|---|---|---|---|---|
| TNF-α | 4 | Linear SVM | 55 | 0.774 | 0.767 | 0.767 | 0.767 | 100.0% | 77.1% |

The model's performance was evaluated through 10-fold cross-validation, illustrating the high classification accuracy achieved for both the training and test sets. In addition, the main hyperparameters after optimization are shown in Table S8.

As shown in Fig. S10, the linear SVM model effectively identified TNF-α under simpler conditions, achieving 100% accuracy in the F12K medium and 78% accuracy in the F12K medium with TNF-α, showing high sensitivity and specificity when no other analytes were present. However, the model struggled in the presence of OSM, with accuracy dropping to 52% in F12K medium with OSM, mainly due to 48% false positives, suggesting spectral overlap or competitive adsorption between OSM and TNF-α. Under these critical conditions, the model often confused the presence of OSM with TNF-α. In F12K medium with both OSM and TNF-α, the model achieved 75% accuracy, performing similarly to the condition with TNF-α alone. Nevertheless, the 25% false negative rate shows that the model sometimes failed to detect TNF-α when OSM was also present, likely due to spectral interference. These results highlight the model's limitation of being trained without OSM-containing spectra, affecting its ability to generalize in complex scenarios. Consistent with OSM analysis, increasing the number of acquired spectra and including OSM-containing spectra in the training set and optimizing SERS surface functionalization could improve the model's ability to distinguish TNF-α in challenging biological environments. Furthermore, exploring deep-learning models for Raman/SERS mixtures (attention/deconvolution and autoencoder-based unmixing), potentially combined with augmentation and transfer/domain adaptation, could improve robustness in complex spectra and across batches.[62–64] Notably, in operational scenarios, rather than relying on single-spectrum predictions, sample-level decisions could be derived by majority voting, which may improve reliability beyond a single spectrum.

### Comparison between the characteristic Raman peaks of OSM and TNF-α *vs.* ML selected features

The identification and selection of Raman peaks for OSM and TNF-α in the context of this study play a critical role in enhancing the model's performance and biological interpretability. By comparing the peaks identified at high analyte concentrations (Tables S1 and S2) with those employed in the optimized ML models, valuable insights into the consistency and relevance of these spectral features were obtained.[30] The identification of common peaks was conducted with a tolerance of ±10 $cm^{-1}$ to account for setup experimental variability and spectral shifts that can arise from pH variations, molecular adsorption geometry, and local SERS enhancement effects. This choice was also made because the most significant differences between classes are often observed on the shoulders of larger peaks, where potentially meaningful variations occur.[30] This approach, as shown in Table 4, ensures accurate and reliable feature selection. For OSM, 21 features of the optimized model (out of 65 total features) were found to be common or closely aligned with peaks identified at high analyte concentrations. These peaks include prominent Raman shifts at 722, 919, 1063, and 1688 $cm^{-1}$, among others. Notably, several of these peaks correspond to molecular vibrations characteristic of amino acids and protein structural elements, such as amide and amino acid signals. For instance, the region around 1688 $cm^{-1}$, associated with amide bonds of disordered structures, highlights the importance of protein

**Table 4** Comparison of characteristic Raman peaks ($cm^{-1}$) of OSM and TNF-α with those used by optimized classifiers. Highlighted values indicate peaks that match between the reference lists (Tables S1 and S2) and the optimized classifiers within ±10 $cm^{-1}$. Peak order follows the original feature identifiers from the ranking and sequential feature selection outputs

| | OSM | TNF-α | | OSM | TNF-α | | OSM | TNF-α |
|---|---|---|---|---|---|---|---|---|
| 1 | 670 | 860 | 23 | 771 | 628 | 45 | 892 | 1061 |
| 2 | 1176 | 790 | 24 | 1049 | 659 | 46 | 693 | 1031 |
| 3 | 1067 | 1204 | 25 | 1688 | 733 | 47 | 1199 | 1324 |
| 4 | 891 | 747 | 26 | 1621 | 1700 | 48 | 1617 | 1191 |
| 5 | 1415 | 905 | 27 | 1421 | 1642 | 49 | 1519 | 915 |
| 6 | 657 | 1035 | 28 | 1687 | 686 | 50 | 1227 | 1084 |
| 7 | 748 | 935 | 29 | 745 | 725 | 51 | 1707 | 1703 |
| 8 | 1422 | 1604 | 30 | 923 | 991 | 52 | 1115 | 950 |
| 9 | 1637 | 962 | 31 | 796 | 814 | 53 | 1229 | 1179 |
| 10 | 1068 | 1332 | 32 | 1192 | 763 | 54 | 621 | 1696 |
| 11 | 1697 | 1657 | 33 | 1193 | 1254 | 55 | 1076 | 1338 |
| 12 | 1638 | 1433 | 34 | 1188 | 698 | 56 | 1245 | — |
| 13 | 698 | 1421 | 35 | 1202 | 1216 | 57 | 1391 | — |
| 14 | 749 | 796 | 36 | 905 | 1047 | 58 | 1319 | — |
| 15 | 1342 | 633 | 37 | 1196 | 801 | 59 | 1317 | — |
| 16 | 1350 | 1618 | 38 | 924 | 1072 | 60 | 1038 | — |
| 17 | 1343 | 1691 | 39 | 1622 | 1314 | 61 | 792 | — |
| 18 | 1387 | 1327 | 40 | 1335 | 951 | 62 | 777 | — |
| 19 | 1351 | 1514 | 41 | 1639 | 765 | 63 | 726 | — |
| 20 | 1046 | 879 | 42 | 1281 | 1041 | 64 | 778 | — |
| 21 | 671 | 967 | 43 | 681 | 1705 | 65 | 1246 | — |
| 22 | 1047 | 1643 | 44 | 1385 | 724 | 66 | — | — |

backbone vibrations in the classification model. Similarly, peaks within the range of 700 to 850 $cm^{-1}$ are attributed to the vibrations of methionine, serine, and tryptophan, which are integral components of the OSM protein's structure. Also, for TNF-α, 21 features of the optimized model (out of 55 total features) were found to be common or closely aligned with peaks identified at high analyte concentrations. These peaks include Raman shifts such as 860, 1204, and 1692 $cm^{-1}$. Notably, the peak at 1692 $cm^{-1}$ aligns with the amide I band, which is indicative of the amide bond, a prominent feature in TNF-α. Additionally, peaks in the range of 700 to 900 $cm^{-1}$, such as 747, 860, and 877 $cm^{-1}$, are associated with the vibrations of amino acids like hydroxyproline, tyrosine, and amino acids containing sulfur. The selective inclusion of these peaks in the optimized model reflects their contribution to differentiating TNF-α-specific spectral features from those of the surrounding matrix. The good overlap of peaks identified in high-concentration studies with those utilized by the ML models demonstrates the robustness of the feature selection process and relies on spectral features that are biologically and chemically meaningful. This consistency enhances the interpretability of the results, providing confidence in the potential application of these SERS-based methods for diagnostic purposes.

## Conclusion

We developed a label-free SERS-based platform integrated into a microphysiological chip with embedded pH tuning for the selective detection of Oncostatin M and TNF-α in Ham's F-12K cell culture medium without serum supplementation. The combination of 3-MPA functionalization and chip-level pH modulation significantly enhanced spectral discrimination and model performance. The optimal detection conditions were identified as pH 6.8 for OSM and pH 4.0 for TNF-α, which corresponded to the most effective analyte–surface interactions and the highest classification accuracy. Of the tested algorithms, a linear Support Vector Machine (SVM) achieved the best overall results, with 79.1% test accuracy for OSM using 65 selected features and 77.1% for TNF-α using 55 selected features. These outcomes demonstrate that coupling SERS signal optimisation with feature-based machine learning enables reliable biomarker discrimination, even in a chemically complex serum-free medium. Although this study focused on a simplified culture medium, the results validate the platform's potential for future applications involving more complex biological fluids and on-chip, cell-based assays. We revealed current limitations under mixed/interferent conditions while demonstrating reliable single-analyte discrimination in a chemically complex serum-free medium, highlighting the platform's potential for future non-invasive biomarker detection in organ-on-chip models. The binary readout based on clinically relevant cut-off concentrations provides a rapid response while also representing a first step toward quantitative approaches. Future work will extend this strategy to additional biomarkers and integrate the chip with cellular models, enabling the real-time monitoring of cytokine secretion and processes such as EMT in dynamic biological environments.

## Author contributions

Daniele Bellisario: conceptualization, data curation, formal analysis, investigation, methodology, visualization, and writing – original draft. Alessandra Calogiuri: conceptualization, data curation, investigation, and writing – original draft. Elisa Sciurti: data curation, formal analysis, investigation, and writing – original draft, review & editing. Laura Blasi: conceptualization, investigation, and writing – original draft, review & editing. Vanessa Esposito: conceptualization, methodology and writing – original draft. Flavio Casino: conceptualization and methodology. Pietro Siciliano: conceptualization, supervision, review & editing. Antonio Della Torre: data curation, formal analysis, investigation, and writing. Luca Francioso: conceptualization, supervision, and writing – original draft, review & editing.

## Conflicts of interest

There are no conflicts to declare.

## Data availability

The data that support the findings of this study are available from the corresponding author upon request.

The supplementary information contains additional SERS spectral data, ELISA and XPS validation results, machine learning methodology details (including feature extraction, model training, and evaluation), classification performance metrics, confusion matrices, optimized hyperparameters, PCA analyses, and supplementary references supporting the main findings of the study. See DOI: https://doi.org/10.1039/d5an00949a.

## Acknowledgements

The author(s) acknowledge financial support for the research, authorship, and/or publication of this article from the European Union – NextGenerationEU, in the context of the National Recovery and Resilience Plan (PNRR), Project Age-It: "Ageing Well in an Ageing Society" (DM 1557, 11 October 2022). The views and opinions expressed are only those of the authors and do not necessarily reflect those of the European Union or the European Commission. Neither the European Union nor the European Commission can be held responsible for them. We gratefully acknowledge Dr Riccardo Di Corato for performing the XPS measurements and for data interpretation.

## References

1 F. Haghayegh, A. Norouziazad, E. Haghani, A. A. Feygin, R. H. Rahimi, H. A. Ghavamabadi, D. Sadighbayan, F. Madhoun, M. Papagelis, T. Felfeli and R. Salahandish, Revolutionary Point-of-Care Wearable Diagnostics for Early Disease Detection and Biomarker Discovery through Intelligent Technologies, *Adv. Sci.*, 2024, **11**, 2400595, DOI: 10.1002/advs.202400595.

2 W. Y. Lim, C.-H. Goh, T. M. Thevarajah, B. T. Goh and S. M. Khor, Using SERS-based microfluidic paper-based device (μPAD) for calibration-free quantitative measurement of AMI cardiac biomarkers, *Biosens. Bioelectron.*, 2020, **147**, 111792, DOI: 10.1016/j.bios.2019.111792.

3 A. N. Resmi, *et al.*, Ultrasensitive Detection of Blood-Based Alzheimer's Disease Biomarkers: A Comprehensive SERS-Immunoassay Platform Enhanced by Machine Learning, *ACS Chem. Neurosci.*, 2024, **15**(24), 4390–4401, DOI: 10.1021/acschemneuro.4c00369.

4 E. K. Sackmann, A. L. Fulton and D. J. Beebe, The present and future role of microfluidics in biomedical research, *Nature*, 2014, **507**(7491), 181–189, DOI: 10.1038/nature13118.

5 E. Sciurti, *et al.*, Label-free electrochemical biosensor for direct detection of Oncostatin M (OSM) inflammatory bowel diseases (IBD) biomarker in human serum, *Talanta*, 2024, **271**, 125726, DOI: 10.1016/j.talanta.2024.125726.

6 C. T. Prontera, *et al.*, Anodic Stripping Voltammetric Determination of Copper Ions in Cell Culture Media: From Transwell® to Organ-on-Chip Systems, *Chemosensors*, 2023, **11**(8), 466, DOI: 10.3390/chemosensors11080466.

7 A. Calogiuri, *et al.*, Non-invasive real-time investigation of colorectal cells tight junctions by Raman microspectroscopy analysis combined with machine learning algorithms for organ-on-chip applications, *Front. Bioeng. Biotechnol.*, 2024, **12**, 1458404, DOI: 10.3389/fbioe.2024.1458404.

8 S. Pahlow, *et al.*, Bioanalytical application of surface– and tip–enhanced Raman spectroscopy, *Eng. Life Sci.*, 2012, **12**(2), 131–143, DOI: 10.1002/elsc.201100056.

9 R. F. Aroca, R. A. Alvarez-Puebla, N. Pieczonka, S. Sanchez-Cortez and J. V. Garcia-Ramos, Surface-enhanced Raman scattering on colloidal nanostructures, *Adv. Colloid Interface Sci.*, 2005, **116**(1–3), 45–61, DOI: 10.1016/j.cis.2005.04.007.

10 A. I. Pérez-Jiménez, D. Lyu, Z. Lu, G. Liu and B. Ren, Surface-enhanced Raman spectroscopy: benefits, trade-offs and future developments, *Chem. Sci.*, 2020, **11**(18), 4563–4577, DOI: 10.1039/D0SC00809E.

11 C. Deriu, S. Thakur, O. Tammaro and L. Fabris, Challenges and opportunities for SERS in the infrared: materials and methods, *Nanoscale Adv.*, 2023, **5**(8), 2132–2166, DOI: 10.1039/D2NA00930G.

12 S. Lian, X. Li and X. Lv, Recent Developments in SERS Microfluidic Chips: From Fundamentals to Biosensing Applications, *ACS Appl. Mater. Interfaces*, 2025, **17**(7), 10193–10230, DOI: 10.1021/acsami.4c17779.

13 L. Ngo, L. Q. A. Pham, A. Tukova, A. Hassanzadeh-Barforoushi, W. Zhang and Y. Wang, Emerging integrated SERS-microfluidic devices for analysis of cancer-derived small extracellular vesicles, *Lab Chip*, 2023, **23**(13), 2899–2921, DOI: 10.1039/D3LC00156C.

14 S. E. Moulton, J. N. Barisci, A. Bath, R. Stella and G. G. Wallace, Investigation of protein adsorption and electrochemical behavior at a gold electrode, *J. Colloid Interface Sci.*, 2003, **261**(2), 312–319, DOI: 10.1016/S0021-9797(03)00073-0.

15 D. Song and D. Forciniti, Effects of Cosolvents and pH on Protein Adsorption on Polystyrene Latex: A Dynamic Light Scattering Study, *J. Colloid Interface Sci.*, 2000, **221**(1), 25–37, DOI: 10.1006/jcis.1999.6560.

16 K. Aoki and T. Kakiuchi, pKa of an ω-carboxylalkanethiol self-assembled monolayer by interaction model, *J. Electroanal. Chem.*, 1999, **478**(1–2), 101–107, DOI: 10.1016/S0022-0728(99)00419-2.

17 G. Lu, T. Z. Forbes and A. J. Haes, SERS detection of uranyl using functionalized gold nanostars promoted by nanoparticle shape and size, *Analyst*, 2016, **141**(17), 5137–5143, DOI: 10.1039/C6AN00891G.

18 L. Guo, *et al.*, Stat3-coordinated Lin-28–let-7–HMGA2 and miR-200–ZEB1 circuits initiate and maintain oncostatin M-driven epithelial–mesenchymal transition, *Oncogene*, 2013, **32**(45), 5272–5282, DOI: 10.1038/onc.2012.573.

19 J. Nightingale, *et al.*, Oncostatin M, a Cytokine Released by Activated Mononuclear Cells, Induces Epithelial Cell-Myofibroblast Transdifferentiation via Jak/Stat Pathway Activation, *J. Am. Soc. Nephrol.*, 2004, **15**(1), 21–32, DOI: 10.1097/01.ASN.0000102479.92582.43.

20 V. A. Luyckx, L. V. Cairo, C. A. Compston, W. L. Phan and T. F. Mueller, Oncostatin M pathway plays a major role in the renal acute phase response, *Am. J. Physiol. Renal Physiol.*, 2009, **296**(4), F875–F883, DOI: 10.1152/ajprenal.90633.2008.

21 B. J. Baker, K. W. Park, H. Qin, X. Ma and E. N. Benveniste, IL-27 inhibits OSM–mediated TNF–α and iNOS gene expression in microglia, *Glia*, 2010, **58**(9), 1082–1093, DOI: 10.1002/glia.20989.

22 R. Sarközi, U. Corazza, J.-P. Osterkamp, M. Pirklbauer, G. Mayer and H. Schramek, Synergistic induction of CCL2/MCP-1 expression driven by oncostatin M and IL-1 $\beta$ in human proximal tubular cells depends on STAT3 and p65 NF $\kappa$ B/RelA, *Physiol. Rep.*, 2015, **3**(2), e12298, DOI: 10.14814/phy2.12298.

23 F. Sun, H. C. Hung and A. Sinclair, *et al., Nat. Commun.*, 2016, **7**, 13437, DOI: 10.1038/ncomms13437.

24 M. S. Schmidt, J. Hübner and A. Boisen, Large Area Fabrication of Leaning Silicon Nanopillars for Surface Enhanced Raman Spectroscopy, *Adv. Mater.*, 2012, **24**, OP11–OP18, DOI: 10.1002/adma.201103496.

25 H. J. Butler, *et al.*, Using Raman spectroscopy to characterize biological materials, *Nat. Protoc.*, 2016, **11**(4), 664–687, DOI: 10.1038/nprot.2016.036.

26 Y. Dong, J. Hu, J. Jin, H. Zhou, S. Jin and D. Yang, Advances in machine learning-assisted SERS sensing towards food safety and biomedical analysis, *TrAC, Trends Anal. Chem.*, 2024, **180**, 117974, DOI: 10.1016/j.trac.2024.117974.

27 A. Ditta, *et al.*, Principal components analysis of Raman spectral data for screening of Hepatitis C infection, *Spectrochim. Acta, Part A*, 2019, **221**, 117173, DOI: 10.1016/j.saa.2019.117173.

28 C. Frausto-Reyes, C. Medina-Gutiérrez, R. Sato-Berrú and L. R. Sahagún, Qualitative study of ethanol content in tequilas by Raman spectroscopy and principal component analysis, *Spectrochim. Acta, Part A*, 2005, **61**(11–12), 2657–2662, DOI: 10.1016/j.saa.2004.10.008.

29 J. Wang, *et al.*, Simultaneous fingerprint and high-wavenumber fiber-optic Raman spectroscopy improves in vivo diagnosis of esophageal squamous cell carcinoma at endoscopy, *Sci. Rep.*, 2015, **5**(1), 12957, DOI: 10.1038/srep12957.

30 J. Yang, *et al.*, Raman spectroscopy for esophageal tumor diagnosis and delineation using machine learning and the portable Raman spectrometer, *Spectrochim. Acta, Part A*, 2024, **317**, 124461, DOI: 10.1016/j.saa.2024.124461.

31 Z. Wang, *et al.*, Rapid Biomarker Screening of Alzheimer's Disease by Interpretable Machine Learning and Graphene-Assisted Raman Spectroscopy, *ACS Nano*, 2022, **16**(4), 6426–6436, DOI: 10.1021/acsnano.2c00538.

32 J. Brank, M. Grobelnik, N. Milic-Frayling and D. Mladenic, Feature Selection Using Linear Support Vector Machines, 2002, Available: https://www.microsoft.com/en-us/research/publication/feature-selection-using-linear-support-vector-machines/.

33 Y.-H. Lee, J. H. Won, Q.-S. Auh and Y.-K. Noh, Age group prediction with panoramic radiomorphometric parameters using machine learning algorithms, *Sci. Rep.*, 2022, **12**(1), 11703, DOI: 10.1038/s41598-022-15691-9.

34 T. Wang, M. Shoaran and A. Emami, Towards Adaptive Deep Brain Stimulation in Parkinson'S Disease: Lfp-Based Feature Analysis and Classification, in *2018 IEEE International Conference on Acoustics, Speech and Signal Processing (ICASSP)*, IEEE, Apr, 2018, pp. 2536–2540. DOI: 10.1109/ICASSP.2018.8462472.

35 S. Lee, *et al.*, Early-stage diagnosis of bladder cancer using surface-enhanced Raman spectroscopy combined with machine learning algorithms in a rat model, *Biosens. Bioelectron.*, 2024, **246**, 115915, DOI: 10.1016/j.bios.2023.115915.

36 R. Kohavi, A study of cross-validation and bootstrap for accuracy estimation and model selection, in *Proceedings of the 14th International Joint Conference on Artificial Intelligence* – Volume 2, in IJCAI'95. San Francisco, CA, USA: Morgan Kaufmann Publishers Inc., 1995, pp. 1137–1143.

37 F. C. Marques, G. P. Oliveira, R. A. R. Teixeira, R. M. S. Justo, T. B. V. Neves and G. F. S. Andrade, Characterization of 11-mercaptoundecanoic and 3-mercaptopropionic acids adsorbed on silver by surface-enhanced Raman scattering, *Vib. Spectrosc.*, 2018, **98**, 139–144, DOI: 10.1016/j.vibspec.2018.07.015.

38 J. V. Santiago, A. Q. Cheeseborough and J. López-Garriga, Hemoglobin I from Lucina pectinata on Collagen Scaffold: A Prospective Hydrogen Sulfide Scavenger, *J. Chem.*, 2022, 1–9, DOI: 10.1155/2022/5101712.

39 A. Tricase, *et al.*, Electrochemical and X-ray Photoelectron Spectroscopy Surface Characterization of Interchain-Driven Self-Assembled Monolayer (SAM) Reorganization, *Nanomaterials*, 2022, **12**(5), 867, DOI: 10.3390/nano12050867.

40 N. Kim, *et al.*, Surface enhanced Raman scattering artificial nose for high dimensionality fingerprinting, *Nat. Commun.*, 2020, **11**, 13615, DOI: 10.1038/s41467-019-13615-2.

41 H. Shin, H. Jeong, J. Park, S. Hong and Y. Choi, Correlation between Cancerous Exosomes and Protein Markers Based on Surface-Enhanced Raman Spectroscopy (SERS) and Principal Component Analysis (PCA), *ACS Sens.*, 2018, **3**(12), 2637–2643, DOI: 10.1021/acssensors.8b01047.

42 S. M. Ansar, X. Li, S. Zou and D. Zhang, Quantitative Comparison of Raman Activities, SERS Activities, and SERS Enhancement Factors of Organothiols: Implication to Chemical Enhancement, *J. Phys. Chem. Lett.*, 2012, **3**(5), 560–565, DOI: 10.1021/jz2016439.

43 I. N. Saraeva, *et al.*, Analysis of Skin Neoplasms' Raman Spectra Using the Lorentz Approximation Method: Pilot Studies, *JETP Lett.*, 2024, **119**(7), 556–563, DOI: 10.1134/S0021364023604153.

44 M. A. Czarnecki, Resolution Enhancement in Second-Derivative Spectra, *Appl. Spectrosc.*, 2015, **69**(1), 67–74, DOI: 10.1366/14-07568.

45 Z. Movasaghi, S. Rehman and I. U. Rehman, Raman Spectroscopy of Biological Tissues, *Appl. Spectrosc. Rev.*, 2007, **42**(5), 493–541, DOI: 10.1080/05704920701551530.

46 G. Pezzotti, Raman spectroscopy in cell biology and microbiology, *J. Raman Spectrosc.*, 2021, **52**(12), 2348–2443, DOI: 10.1002/jrs.6204.
47 N. Kuhar, S. Sil and S. Umapathy, Potential of Raman spectroscopic techniques to study proteins, *Spectrochim. Acta, Part A*, 2021, **258**, 119712, DOI: 10.1016/j.saa.2021.119712.
48 J. Guicheteau, L. Argue, A. Hyre, M. Jacobson and S. D. Christesen, Raman and surface-enhanced Raman spectroscopy of amino acids and nucleotide bases for target bacterial vibrational mode identification, Proc. SPIE 6218, Chemical and Biological Sensing VII, 62180O, 2006. DOI: 10.1117/12.670294.
49 P. D. C. Gomes, M. Hardy, Y. Tagger, J. J. S. Rickard, P. Mendes and P. G. Oppenheimer, Optimization of Nanosubstrates toward Molecularly Surface-Functionalized Raman Spectroscopy, *J. Phys. Chem. C*, 2022, **126**(32), 13774–13784, DOI: 10.1021/acs.jpcc.2c03524.
50 S. Bhunia, S. K. Srivastava, A. Materny and A. K. Ojha, A vibrational and conformational characterization of arginine at different pH values investigated using Raman spectroscopy combined with DFT calculations, *J. Raman Spectrosc.*, 2016, **47**(9), 1073–1085, DOI: 10.1002/jrs.4918.
51 M. Kazanci, J. P. Schulte, C. Douglas, P. Fratzl, D. Pink and T. Smith-Palmer, Tuning the Surface-Enhanced Raman Scattering Effect to Different Molecular Groups by Switching the Silver Colloid Solution pH, *Appl. Spectrosc.*, 2009, **63**(2), 214–223, DOI: 10.1366/000370209787391987.
52 V. Mollica Nardo, V. Renda, S. Trusso and R. C. Ponterio, Role of pH on Nanostructured SERS Active Substrates for Detection of Organic Dyes, *Molecules*, 2021, **26**(8), 2360, DOI: 10.3390/molecules26082360.
53 S. C. Burris, Y. Zhou, W. A. Maupin, A. J. Ebelhar and M. W. Daugherty, The Effect of Surface Preparation on Apparent Surface pKa's of ω-Mercaptocarboxylic Acid Self-Assembled Monolayers on Polycrystalline Gold, *J. Phys. Chem. C*, 2008, **112**(17), 6811–6815, DOI: 10.1021/jp077052w.
54 H. T. M. Phan, S. Bartelt-Hunt, K. B. Rodenhausen, M. Schubert and J. C. Bartz, Investigation of Bovine Serum Albumin (BSA) Attachment onto Self-Assembled Monolayers (SAMs) Using Combinatorial Quartz Crystal Microbalance with Dissipation (QCM-D) and Spectroscopic Ellipsometry (SE), *PLoS One*, 2015, **10**(10), e0141282, DOI: 10.1371/journal.pone.0141282.
55 W. A. Marmisollé, D. A. Capdevila, E. de la Llave, F. J. Williams and D. H. Murgida, Self-Assembled Monolayers of $NH_2$-Terminated Thiolates: Order, p$K_a$, and Specific Adsorption, *Langmuir*, 2013, **29**(17), 5351–5359, DOI: 10.1021/la304730q.
56 W. Sanders and M. R. Anderson, Potential Driven Deposition of Poly(diallyldimethylammonium chloride) onto the Surface of 3-Mercaptopropionic Acid Monolayers Assembled on Gold, *Langmuir*, 2008, **24**(22), 12766–12770, DOI: 10.1021/la801512g.
57 N. Blake, R. Gaifulina, L. D. Griffin, I. M. Bell and G. M. H. Thomas, Machine Learning of Raman Spectroscopy Data for Classifying Cancers: A Review of the Recent Literature, *Diagnostics*, 1491, **12**, 6, DOI: 10.3390/diagnostics12061491.
58 S. Guo, T. Bocklitz, U. Neugebauer and J. Popp, Common mistakes in cross-validating classification models, *Anal. Methods*, 2017, **9**(30), 4410–4417, DOI: 10.1039/C7AY01363A.
59 E. B. Huerta, R. M. Caporal, M. A. Arjona and J. C. H. Hernández, *Recursive Feature Elimination Based on Linear Discriminant Analysis for Molecular Selection and Classification of Diseases*, 2013, pp. 244–251. DOI: 10.1007/978-3-642-39482-9_28.
60 S. Abdanan Mehdizadeh, M. Noshad and M. Hojjati, A modified sequential wavenumber selection-discriminant analysis with Bayesian optimization strategy for detection and identification of chia seed oil adulteration using Raman spectroscopy, *Talanta*, 2024, **277**, 126439, DOI: 10.1016/j.talanta.2024.126439.
61 A. Nakar, A. Pistiki, O. Ryabchykov, T. Bocklitz, P. Rösch and J. Popp, Detection of multi-resistant clinical strains of *E. coli* with Raman spectroscopy, *Anal. Bioanal. Chem.*, 2022, **414**(4), 1481–1492, DOI: 10.1007/s00216-021-03800-y.
62 D. Georgiev, Á. Fernández-Galiana, S. Vilms Pedersen, G. Papadopoulos, R. Xie, M. M. Stevens and M. Barahona, Hyperspectral unmixing for Raman spectroscopy via physics-constrained autoencoders, *Proc. Natl. Acad. Sci. U. S. A.*, 2024, **121**(45), e2407439121, DOI: 10.1073/pnas.2407439121.
63 Z. Bu, J. Liu, J. Zhang, C. Liu, Y. Liu, K. Ren, X. Yan, W. Gao and J. Dong, Deep learning-driven components analysis of Raman spectral mixtures: An integrated masked autoencoder with convolutional neural network approach, *Chemom. Intell. Lab. Syst.*, 2026, **269**, 105627, DOI: 10.1016/j.chemolab.2025.105627.
64 M. Kazemzadeh, C. L. Hisey, K. Zargar-Shoshtari, W. Xu and N. G. R. Broderick, Deep convolutional neural networks as a unified solution for Raman spectroscopy-based classification in biomedical applications, *Opt. Commun.*, 2022, **510**, 127977, DOI: 10.1016/j.optcom.2022.127977.